A reduced complexity ECG imaging model for regularized inversion optimization

Maureen Manche, Karim El Houari, Amar Kachenoura, Laurent Albera, Michel Rochette, Alfredo Hernandez, Saïd Moussaoui

A reduced complexity ECG imaging model for regularized inversion optimization

Maureen MANCHE[a,b,*], Karim EL HOUARI[c,*], Amar KACHENOURA[a,**], Laurent ALBERA[a], Michel ROCHETTE[c], Alfredo HERNÁNDEZ[a] and Saïd MOUSSAOUI[b]

[a] *University of Rennes (LTSI), Inserm - UMR 1099, Rennes, 35000, France*
[b] *Nantes Université, Ecole Centrale Nantes, LS2N UMR CNRS 6004, Nantes, 44000, France*
[c] *ANSYS SAS., Villeurbane, 69100, France*

ARTICLE INFO

Keywords:
3D heart-torso phenomenological model
Electrocardiography inverse problem
Hyperparameter identification
Sensitivity analysis

ABSTRACT

The resolution of the inverse problem of electrocardiography represents a major interest in the diagnosis and catheter-based therapy of cardiac arrhythmia. In this context, the ability to simulate several cardiac electrical behaviors was crucial for evaluating and comparing the performance of inversion methods. For this application, existing models are either too complex or do not produce realistic cardiac patterns. In this work, a low-resolution heart-torso model generating realistic whole heart cardiac mappings and electrocardiograms in healthy and pathological cases is designed. This model was built upon a simplified heart-torso geometry and implements the monodomain formalism by using the finite element method. In addition, a model reduction step through a sensitivity analysis was proposed where parameters were identified using an evolutionary optimization approach. Finally, the study illustrates the usefulness of the proposed model by comparing the performance of different variants of Tikhonov-based inversion methods for the determination of the regularization parameter in healthy, ischemic and ventricular tachycardia scenarios. First, results of the sensitivity analysis show that among 58 parameters only 25 are influent. Note also that the level of influence of the parameters depends on the heart region. Besides, the synthesized electrocardiograms globally present the same characteristic shape compared to the reference once with a correlation value that reaches 88%. Regarding inverse problem, results highlight that only Robust Generalized Cross Validation and Discrepancy Principle provide best performance, with a quasi-perfect success rate for both, and a respective relative error, between the generated electrocardiograms to the reference one, of 0.75 and 0.62.

1. Introduction

Cardiovascular diseases are the leading cause of mortality worldwide and represent a huge health and economic burden [1]. Most of these deaths are due to heart failure caused by an abnormal propagation of electrical activity within the heart, a phenomenon referred to as cardiac arrhythmia. In the treatment of cardiac arrhythmia, catheter ablation revealed itself as the only curative alternative in contrast to lifelong medication or implantable cardioverter defibrillator. In this minimally invasive procedure, a mapping catheter is inserted through blood vessels and is moved inside the heart in order to record local electrical cardiac activity. This allows us to delineate the arrhythmogenic target, which is then ablated by delivering radio-frequency energy. Although successful ablation eliminates arrhythmia, the recurrence rate is still high [2], and the several-hours surgical procedures are tedious for both patients and surgeons.

In this connection, ECG Imaging (ECGI) is an emerging non-invasive modality for an appropriate diagnosis and a better-guided ablation procedure. It consists in computing 3D mappings of cardiac electrical activity based on anatomical data obtained from magnetic resonance or tomography scans, and ECG recordings on the torso surface. Although very promising, one major issue with ECGI is that validation using in vivo human data is made difficult. Indeed, while in vivo studies were conducted in animals [3, 4], simultaneous whole heart electrical mappings are unavailable for patients in practice. For this reason, cardiac computational models play the essential role of providing numerical simulations of ground truth electrical data in order to evaluate and compare existing ECGI inversion algorithms. They also contribute to a better understanding of arrhythmogenesis through simulation.

*Maureen Manche and Karim El Houari contributed equally to this work.
**Corresponding author. E-mail address: amar.kachenoura@univ-rennes.fr
ORCID(s): 0009-0003-8441-5296 (M. MANCHE)

Within the framework of evaluating reconstruction algorithms using model-based data, a convenient model should be able to generate sufficiently realistic cardiac patterns that produce meaningful surface ECGs, with sufficiently low complexity in order to consider various ECGI case scenario simulations. Numerous ECGI studies and cardiac models can be found in the literature. Many works were devoted to represent cardiac behavior with a high level of detail including fiber orientation [5], high-resolution meshes [6], novel heart-torso coupling techniques [7] and anatomically detailed geometries [8]. In [9] authors proposed a simplified heart-torso model geometry in the case of sinus-rhythm. More recently, the parameters of this model were tuned in [10] to reproduce pathological cases in the context of a closed loop tool for the simulation and assessment of pacemakers. Another work [11] proposes a novel torso-heart model of personal electrophysiology, embedded in a real-time cardiac simulator, with precise anatomical and structural representations of atria and ventricles. Moreover, all these studies are based on the bidomain formalism. In addition, the models proposed in [5] and [8] only include ventricles, whereas [6, 7, 9, 10, 11] proposed a whole cardiac model. However, when the goal is to evaluate, compare performance and study parameters influence on ECGI algorithms, these models are not suited since they are far too complex. Moreover, only few cardiac models are able to synthesize a complete and meaningful set of 12-Lead ECG signals, which is a key issue for understanding the relationship between the torso surface ECGs and cardiac electrical dynamics.

The other major issue with ECGI is that recovering electrical potentials in the heart domain from few, attenuated measurements on the torso surface is an ill-posed inverse problem. Indeed, the solution is not unique and small perturbations on the measured ECGs entail large changes in the estimated solution. The common approach to tackle this problem is the so-called Tikhonov regularization. This consists in finding the best fit to data solution in the least squares sense whereas considering an additional penalty term to constrain the solution space. This introduces a regularization parameter to be determined that balances between the amount of data fidelity and regularization, and whose value has a major effect on the solution.

This work addresses both the modeling part related to the forward problem by proposing a novel model dedicated to conduct ECGI simulations and to evaluate inversion methods. First, the framework for building a simplified, fast and scalable heart-torso propagation model was presented. The model implements the adapted monodomain formalism, which is a modification of the bidomain approach with lower complexity [12]. The monodomain model is coupled with the phenomenological FitzHugh-Nagumo (FHN) model for describing transmembrane currents. This model includes both atria and ventricles, and the parameters are assigned to different values at each region of the cardiac conduction system. A first step consists in identifying the most influential parameters through a Morris screening sensitivity analysis [13]. Then, the set of model parameters was reduced and the most sensitive ones are estimated through an evolutionary algorithm. The identification process was performed in such a way that the ECG synthesized by the proposed model was the closest to a reference ECG. Following this framework, the presented model was able to synthesize meaningful normal and pathological ECGs whereas keeping a reasonable level of numerical complexity. In a second step, it was shown how the new model can help to evaluate the performance of ECGI methods. More particularly, a comparative study of classical methods devoted to the choice of the adequate penalty parameter in Tikhonov regularization was given. As proposed in [14] the U-curve [15], the Composite Residual and Smoothing Operator (CRESO) [16], the Generalized Cross Validation (GCV) [17] and the Robust Generalized Cross Validation (RGCV) [18] methods are considered. These approaches are also compared with the classical L-curve algorithm [19] and the Discrepancy Principle (DP) [20].

The remainder of this paper is organized as follows. The methodological aspects of the work are addressed in Section 2 and it is divided into three subsections. The first one presents the considered geometry, the equations of cardiac electrical propagation and their coupling to torso potentials. The second subsection describes the model reduction step using Morris sensitivity analysis, the formulation of the parameter identification problem and its resolution using an evolutionary optimization algorithm. The third subsection presents classical methods for choosing the regularization parameter for solving the ECG inverse problem using Tikhonov regularization. Section 3 presents some numerical results in terms of cardiac potentials, propagation patterns and resulting ECG signals, as well as performance of inversion approaches. Finally, section 4 provides an overall discussion on the work and gives some perspectives.

2. Materials and methods

This section presents the methodological framework that was followed in order to produce ECGs from the proposed simplified 3D heart-torso model. First, the designed geometry was described as well as the model equations used to

simulate cardiac propagation and surface ECG measurements. The set of parameters on which the model depends was then reduced by a sensitivity analysis. Finally, an optimization process was used to simulate realistic ECGs and cardiac propagation patterns.

2.1. Heart-torso model

2.1.1. Geometry and meshing

Inspired by [9], a new 3D geometry of heart-torso model (Fig. 1) was designed. It consists of an elliptic-shaped torso and lungs, and an ellipsoid heart that contains the main cardiac regions of the cardiac conduction system: atria, Atrio-Ventricular Node (AVN), bundle of His, bundle branches, endocardium/Purkinje Fibers (PF) and ventricles (midmyocardium and epicardium). Since electrical connection between atria and ventricles is only allowed through the AVN in the real heart, an empty space was created between the two chambers. Blood chambers and the valve plane were considered as vacuum when simulating cardiac propagation. An isotropic but regionally heterogeneous structure representation was integrated, without adding fiber orientation information. Anatomical meshes of the torso, the lungs and the seven regions of the heart were generated from volumetric segmentations using ANSYS DesignModeler software [21] after a series of elementary operations. It was then exported to ANSYS Mechanical [22] in which a meshing step was performed in order to solve numerically the forward problem.

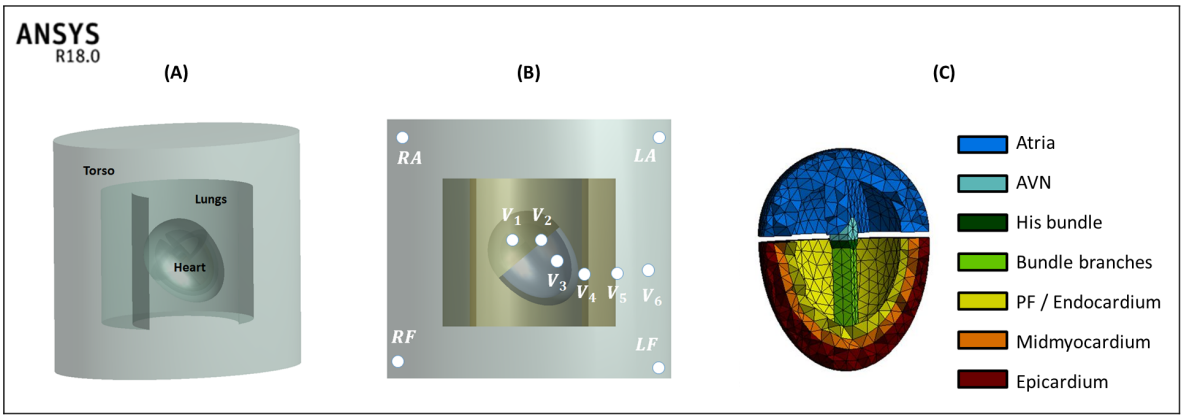

Figure 1: (A) 3D heart-torso geometry of the model, (B) 12-Lead ECGs electrode configuration, (C) Heart mesh and its seven regions, using ANSYS software

A major improvement in the used geometry in contrast with [9] is that a third layer at the ventricular level was added to distinguish the epicardium, midmyocardium, and endocardium. In fact, the difference in electrical properties of ventricular action potentials from the inner and outer layers is a major point to the generation of appropriate ECG signals, and particularly the T-wave. More precisely, action potentials duration diminishes smoothly as one moves from the outer layer to the inner layer of the heart. This gives the effect of a repolarization wavefront traveling from the outside to the inside of the heart, contrarily to depolarization.

2.1.2. Model equations

The bidomain and the monodomain models are widely used to simulate cardiac electrical propagation in current research and are largely accepted for their physiological relevance. The bidomain theory is based on the assumption that cardiac tissue can be partitioned into two separate conducting media: the intracellular space, located inside the cardiac cells, and the extracellular space that connects cells between them. These two spaces are separated by the cell membranes, through which current flows from one space to another. At the macroscopic scale, a homogenization process [23, 24] of the bidomain model considers that these two spaces overlap so that each point of the 3D cardiac space has intracellular and extracellular variables. The bidomain model arises from Maxwell's equations under quasi-static conditions. Indeed, considering the size of the human torso and the range of physiological variables in it, the temporal dynamics of electromagnetic fields can largely be ignored. The full heart-torso bidomain model is made up of a reaction-diffusion equation ((1) and (2)) coupled with an elliptic equation that involves cardiac and extracardiac variables. Alternatively, the monodomain model approximates the bidomain based on an equal anisotropy assumption in the myocardium. This approximation lies in the existence of a constant ratio β between the extracellular conductivity

$\boldsymbol{\sigma}_{ex}$ and the intracellular conductivity $\boldsymbol{\sigma}_{in}$ everywhere in the heart volume. This assumption has no physiological meaning, but is convenient in the sense that computations in the heart and in the torso are decoupled, while providing close results to that of the bidomain. The equations of the monodomain model in the heart domain are given by:

$$\frac{\beta}{1+\beta}\nabla\cdot(\boldsymbol{\sigma}_{in}\nabla v_m) = \chi(c_m\frac{\partial v_m}{\partial t} + i_{ion}(v_m,u) + i_{stim}) \tag{1}$$

$$\nabla\cdot(\boldsymbol{\sigma}_{in}\nabla v_m) + (\beta+1)\nabla\cdot(\boldsymbol{\sigma}_{in}\nabla\phi_{ex}) = 0 \tag{2}$$

where the operators ∇ and $\nabla\cdot$ denote the gradient and the divergence operators respectively. The first equation is a reaction-diffusion equation that translates the spatio-temporal propagation of the transmembrane action potential v_m in the myocardium, where v_m is by definition the potential difference between the intracellular and the extracellular medium, c_m is the membrane capacitance, χ is the surface to volume ratio representing how much membrane surface area is present per volume of cardiac tissue. i_{stim} is a stimulation current that is only non-zero in the chosen region from which propagation is initiated and i_{ion} the ionic currents exchanged between the two media. The elliptic equation (2) expresses the conservation of charge across the complete cardiac domain and links transmembrane v_m and extracellular potentials ϕ_{ex}. This system is completed with an ordinary differential equation satisfied by the ionic variable u in order to describe the evolution of ionic currents $i_{ion}(v_m,u)$:

$$\frac{\partial u}{\partial t} + f(v_m,u) = 0 \tag{3}$$

where f is a scalar function that links variables v_m and u. An appropriate choice for defining f and $i_{ion}(v_m,u)$ is required in (1) and (3). Since physiological models are too complex to conduct whole heart simulations for the intended application, phenomenological models are used instead. The oscillatory FitzHugh-Nagumo (FHN) model [25] adds only one ODE equation of the type (3) to the system. It is continuous, analytically tractable and presents interesting existence and uniqueness properties [26, 27, 28]. In addition, it presents the nice advantage of a graphical analysis of its dynamics using a phase plane representation [29]. Moreover, it is capable of precisely fitting physiological action potentials and has been successfully used in 3D cardiac propagation models [9, 30, 31]. Within the FHN framework, function $f(v_m,u)$ in (3) and the term $i_{ion}(v_m,u)$ in (1) are defined as follows:

$$f(v_m,u) = -ke\left(\frac{v_m-b_2}{a_2} - du - b_1\right), \tag{4}$$

$$i_{ion}(v_m,u) = kc_1(v_m-b_2)\left(a_1-\frac{v_m-b_2}{a_2}\right)\left(1-\frac{v_m-b_2}{a_2}\right) + kc_2u(v_m-b_2) \tag{5}$$

where $a_1, a_2, b_1, b_2, c_1, c_2, d, e$ and k, are non-physiological parameters, but their tuning can result in characteristic shapes of cardiac action potentials of different tissues [32]. This system of equations is completed by the Laplace equation in the passive torso, and boundary conditions that express the coupling between heart and torso:

$$\boldsymbol{n}_{\partial\mathcal{H}}\cdot(\boldsymbol{\sigma}_{in}\nabla v_m) = 0 \tag{6}$$

$$\nabla\cdot(\boldsymbol{\sigma}_t\nabla\phi_t) = 0 \tag{7}$$

$$\boldsymbol{n}_{\partial\mathcal{T}}\cdot(\boldsymbol{\sigma}_t\nabla\phi_t) = 0 \tag{8}$$

$$\phi_t = \phi_{ex} \tag{9}$$

$$\boldsymbol{n}_{\partial\mathcal{H}}\cdot(\boldsymbol{\sigma}_t\nabla\phi_t) = \boldsymbol{n}_{\partial\mathcal{H}}\cdot(\boldsymbol{\sigma}_{ex}\nabla\phi_{ex}) \tag{10}$$

where $\boldsymbol{n}_{\partial\mathcal{H}}$ is the outward pointing normal to the heart surface, the symbol $\cdot$ denotes the inner product, $\boldsymbol{\sigma}_t$ and $\boldsymbol{\phi}_t$ are respectively the extra-cardiac conductivity and the extra-cardiac electrical potential, and $\boldsymbol{n}_{\partial\mathcal{T}}$ is the outward pointing normal to the torso surface.

The Finite Element Method (FEM) was employed to discretize the system in space and an implicit Euler scheme for temporal discretization. Equations (1) and (3) result in the following system to be solved at each time step in the heart domain for the discretized versions of u and v_m:

$$\boldsymbol{u}^{(n+1)} = \boldsymbol{u}^{(n)} - \boldsymbol{f}(\boldsymbol{v}_m^{(n)},\boldsymbol{u}^{(n)}) \tag{11}$$

$$\boldsymbol{D}_{\chi c_m}\boldsymbol{v}_m^{(n)} - \Delta t\boldsymbol{D}_{\chi}(i_{ion}(\boldsymbol{v}_{\boldsymbol{m}}^{(n)},\boldsymbol{u}^{(n+1)}) + \boldsymbol{i}_{stim}) = \left(\Delta t\frac{\beta}{1+\beta}\boldsymbol{A}_{\sigma_{in}} + \boldsymbol{D}_{\chi c_m}\right)\boldsymbol{v}_m^{(n+1)} \tag{12}$$

where $\boldsymbol{u}^{(n+1)}$ and $\boldsymbol{v}_m^{(n+1)}$ are vector versions of u and v_m at time $n+1$, whose i^{th} component corresponds to the values u and v_m at node i of the heart mesh. $\boldsymbol{A}_{\sigma_{in}}$ is the so-called stiffness matrix, and $\boldsymbol{D}_{\chi}$ and $\boldsymbol{D}_{\chi c_m}$ are the so-called damping matrices [33]. In order to solve the PDE system (11) and (12) at each time step $n+1$, an appropriate initialization and an initial stimulation needs to be applied to initiate the propagation process. To do so, the stimulation current i_{stim} is applied on a chosen node i_{san} in the exterior wall of the right atrium as the Sino-Atrial Node (SAN) region of the designed heart. The complete procedure for solving the PDE system is given in Algorithm 1.

Algorithm 1 Algorithm for computing v_m based on the monodomain formalism

Initialization:

$$\boldsymbol{v}_m^{(0)} = \boldsymbol{v}_m^0, \boldsymbol{u}^{(0)} = \boldsymbol{u}^0, \boldsymbol{i}_{stim} = \boldsymbol{0}, \boldsymbol{i}_{stim}(i_{san}) \neq 0$$

Assemble matrices $\boldsymbol{A}_{\sigma_{in}}$, $\boldsymbol{D}_{\chi c_m}$ and $\boldsymbol{D}_{\chi}$

Compute the system matrix $\boldsymbol{A} = \Delta t \frac{\beta}{1+\beta} \boldsymbol{A}_{\sigma_{in}} + \boldsymbol{D}_{\chi c_m}$

for $n = 1 : T$ **do**

  if $n\Delta t > t_{stim}$ **then**

    $i_{stim}(i_{san}) = 0$

  end if

  $u_i^{(n+1)} = u_i^{(n)} + \Delta t k e \left(\frac{v_{m_i}^{(n)} - b_2}{a_2} - d u_i^{(n)} - b_1 \right) \forall i \in \mathcal{M}_{\mathcal{H}}$

  $\boldsymbol{b} = \boldsymbol{D}_{\chi c_m} \boldsymbol{v}_m^{(n+1)} - \Delta t \boldsymbol{D}_{\chi} \left(i_{ion}(\boldsymbol{v}_m^{(n)}, \boldsymbol{u}^{(n+1)}) + \boldsymbol{i}_{stim} \right)$

  Solve $\boldsymbol{A} \boldsymbol{v}_m^{(n+1)} = \boldsymbol{b}$ through Cholesky factorization

end for

$\mathcal{M}_{\mathcal{H}}$ is the set of nodes indexes in the heart.

Now that transmembrane potentials $\boldsymbol{v_m}$ are available, the computation of extracellular potentials within the myocardium and those of the rest of the volume can be completed. Multiplying $\frac{\beta}{1+\beta}$ to (2) and adding (7) reflects the charge conservation in the whole heart-torso domain:

$$\nabla \cdot (\boldsymbol{\sigma}_t \nabla \phi_t) + \frac{\beta}{1+\beta} \nabla \cdot (\boldsymbol{\sigma}_{in} \nabla v_m) + \beta \nabla \cdot (\boldsymbol{\sigma}_{in} \nabla \phi_{ex}) = 0 \tag{13}$$

The discretization process leads to a linear system linking cardiac transmembrane potentials and potentials in the whole heart-torso domain:

$$\boldsymbol{A}_{\bar{\sigma}} \begin{bmatrix} \boldsymbol{\phi}_{ex}^{(n)} \\ \boldsymbol{\phi}_t^{(n)} \end{bmatrix} = \frac{\beta}{1+\beta} \begin{bmatrix} -\boldsymbol{A}_{\sigma_{in}} \boldsymbol{v}_m^{(n)} \\ \boldsymbol{0} \end{bmatrix} \tag{14}$$

where $\boldsymbol{\phi}_{ex}^{(n)}$ and $\boldsymbol{\phi}_t^{(n)}$ are the discretized versions of the continuous variables ϕ_{ex} and ϕ_t respectively, and where $\boldsymbol{A}_{\bar{\sigma}}$ is the stiffness matrix of the whole heart-torso volume. $\bar{\boldsymbol{\sigma}}$ is an equivalent conductivity that equals $\beta \boldsymbol{\sigma}_{in}$ in $\mathcal{H}$ and $\boldsymbol{\sigma}_t$ in $\mathcal{T}$.

The solution of the system (14) can be only determined to within an arbitrary additive constant. Indeed, $\boldsymbol{A}_{\bar{\sigma}}$ is one-rank deficient and its kernel is given by the space of uniformly valued vectors. A physical explanation is that any uniform potential distribution over the entire domain satisfies the conservation law since the resulting current equals zero. To overcome this problem, one solution is to set a potential reference at a chosen node of the volume mesh, which reduces the system size (originally $N \times N$) to $(N-1) \times (N-1)$. Finally, the standard 12-Lead ECGs are computed from the values of $\boldsymbol{\phi}_t$.

2.2. Model reduction & parameter identification

2.2.1. Optimization problem formulation

Model parameter description: Although the FHN model is a controllable oscillatory tool for generating various action potential shapes in the isolated cell, it is another matter when integrated in a 3D reaction-diffusion model. The number of parameters is high and their manual tuning is laborious. An automatic procedure to define parameter values of the whole model, that produce ECGs that are close to a known sinus-rhythm reference ECG, was proposed. The ECG signal can be decomposed into three waves resulting directly from the cardiac depolarization and repolarization

wavefronts: the P wave, the QRS complex and the T wave that have known characteristics in the case of normal rhythm. This can help defining a measure of correctness of the ECGs simulated by our model. Let us denote by $\boldsymbol{p}$ the set of parameters to identify, namely the FHN model parameters defined in (5) and (4), completed with c_m, the conductivity of each region, and χ:

$$\boldsymbol{p} = \left\{\boldsymbol{\sigma}_{ini}, \chi, c_{mi}, a_{1i}, a_2, b_{1i}, c_{1i}, c_{2i}, d_i, e_i, k_i\right\}$$

where i is the index of the considered region. It is noteworthy since the new design model is isotropic and regionally homogeneous, the conductivity tensor $\boldsymbol{\sigma}_{ini}$ reduces to a scalar parameter to be identified for each region, namely atria, AVN, bundle of His, bundle branches, endocardium/PF, midmyocardium and epicardium. Regarding the parameters a_2 and χ, they are assumed to take the same value for all regions of the heart. In fact, χ is the surface to volume ratio. It is more related to the mesh resolution rather than cardiac regional characteristics. Regarding a_2, the justification comes from the fact that this parameter regulates action potentials amplitude, which is supposed to be roughly the same (around 30mV) everywhere in the healthy heart. The equal anisotropy parameter β is not identified. Indeed, it is a scaling factor that is independent from space and thus the considered region, and whose influence is absorbed in the value of $\boldsymbol{\sigma}_{in}$. Moreover, the epicardium parameters have been forced to take the same values as those of the endocardium, with the exception of parameter e, which primarily regulates action potential duration. This parameter is denoted e_{epi} for the epicardium. Indeed, it is assumed that the potentials of inner and outer layer of the epicardium to be of the same shape but with different durations. The resting potential parameter b_{2i} is fixed to $-85mV$ for all regions.

The proposed cost function: An appropriate cost function needs to be defined in order to solve the underlying optimization problem. Our approach consists in maximizing a similarity measure between a real ECG denoted ecg^I_{ref} and the one simulated by our model $ecg^I(\boldsymbol{p})$, constrained by the signal waves durations and relative amplitudes. Then, a suitable cost function, based on the normalized scalar product between the two signals, was defined. Apart from providing a similarity measure, this choice also overcomes scaling issues. Equality constraints are imposed based on features measured on the target ECG. The chosen features are: the durations of the P wave (c_1^{ref}), those of the QRS complex (c_2^{ref}), those of the T wave (c_3^{ref}), those of the PR interval (c_4^{ref}), the maximum peak amplitude ratios between the QRS complex and the P wave (c_5^{ref}), and that between the QRS complex and the T wave (c_6^{ref}). Fig. 2 shows the reference ECG and the corresponding features.

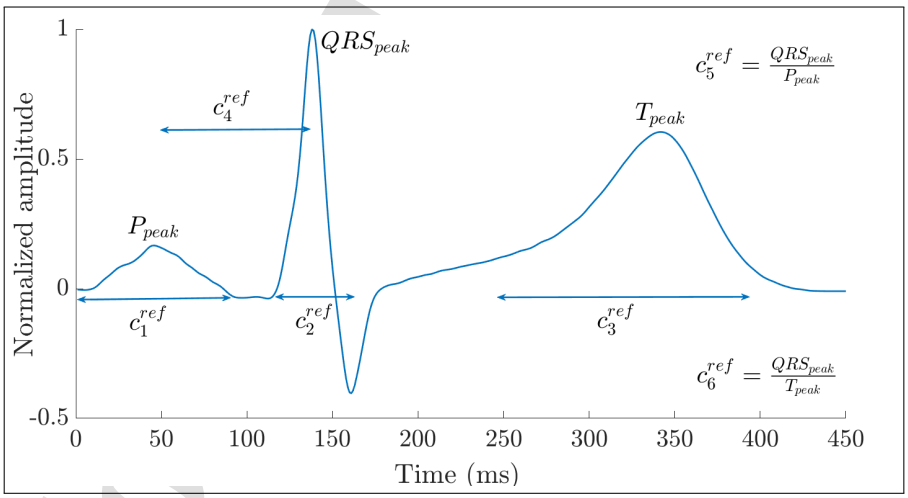

Figure 2: Target ECG signal and its features (lead I)

The optimization problem can then be expressed as follows:

$$\boldsymbol{p}^* = \underset{\boldsymbol{p}}{\operatorname{argmin}} \left(1 - \frac{|\left\langle ecg_I(\boldsymbol{p}), ecg_I^{ref}\right\rangle|}{||ecg_I(\boldsymbol{p})||_2 ||ecg_I^{ref}||_2}\right)^2 \tag{15}$$

$$\text{s.t.:} \qquad \boldsymbol{c}(\boldsymbol{p}) = \boldsymbol{c}^{ref}$$

where $\langle \cdot, \cdot \rangle$ and $\| \cdot \|_2$ denote the inner product and the ℓ_2-norm respectively. $\boldsymbol{c}^{ref} = [c_1^{ref} ... c_6^{ref}]$ is the vectorized form of the features defined above, and $\boldsymbol{c}(\boldsymbol{p})$ those measured on the simulated ECG with parameter set $\boldsymbol{p}$. The minimization problem (15) can be re-expressed as the unconstrained minimization of a modified Lagrangian function defined by:

$$\mathcal{L}(\boldsymbol{p}, \alpha) \quad = \quad \left(1 - \frac{(< ecg_I(\boldsymbol{p}), ecg_I^{ref} >)}{||ecg_I(\boldsymbol{p})||_2 ||ecg_I^{ref}||_2}\right)^2 + \sum_{i=1}^{6} \alpha_i (c_i(\boldsymbol{p}) - c_i^{ref})^2 \tag{16}$$

where the so-called Lagrange multipliers $\alpha = (\alpha_i)_{i \in \{1,...,6\}}$ were empirically fixed at values that ensure the same order of magnitude between these non-homogenous constraints.

2.2.2. Model reduction

Since the proposed model depends on many non-physiological parameters whose influence may be negligible in the simulation of cardiac propagation, it is of interest to perform a sensitivity analysis of the presented model with respect to its input parameters. This way, the parameter set on which the model depends can be reduced in order to only keep parameters that are the most influential in the parameter identification process. Among sensitivity methods, screening approaches consider several inputs configuration and evaluate the effects on the outputs when elementary perturbations are applied on the inputs, for each configuration. Thus, they present the advantage to provide information about how model parameters influence the outputs and how they interact with each other, with a reasonable computational cost. One of the simplest and most popular screening approaches is the Morris method [13]. It is a one at the time approach that is well adapted when the model depends on a high number of parameters. Let us consider the model output $\mathcal{L}$ that depends on the set of parameters $\boldsymbol{p} = (p_1, p_2, ..., p_P)$, a regular grid that partitions each parameter variation domain into L levels, and an elementary displacement δ in the grid that is the same for all parameters. The first step of the method is to define random trajectories in the parameter space in which only one parameter at the time is varied. This consists in sampling a random point $\boldsymbol{p}^{(0)}$ in the defined grid. From this point, only one parameter $p_i^{(0)}, i \in \{1, ..., P\}$ is varied by δ to create a new point $\boldsymbol{p}^{(1)}$. From $\boldsymbol{p}^{(1)}$ this operation is performed for the remaining parameters. This results in $P + 1$ points such that only one parameter varies between $\boldsymbol{p}^{(i-1)}$ and $\boldsymbol{p}^{(i)}$. This scheme is then repeated for $R - 1$ different starting points so that Ψ trajectories are created. Thus, for different parameter sets $\boldsymbol{p}^{(i,j)} (i \in \{0, ..., P\}, j \in \{1, ..., \Psi\})$, the computational cost for the Morris method is given by $\Psi \times (P + 1)$. The second step consists in evaluating each of the created parameter sets by the model and computing output variations corresponding to elementary displacements. The variation of the model output for an elementary displacement in parameter p_i ($i \in \{1, ..., P\}$) in the j^{th} trajectory ($j \in \{1, ..., \Psi\}$) is given by:

$$d^{(i,j)} = \mathcal{L}(\boldsymbol{p}^{(k_i,j)}) - \mathcal{L}(\boldsymbol{p}^{(k_i-1,j)}) \tag{17}$$

where k_i and $k_i - 1$ are the indexes for which only p_i varied between $\boldsymbol{p}^{k_i-1,j}$ and $\boldsymbol{p}^{k_i,j}$. The third step consists in computing the mean μ_i and standards deviation σ_i of elementary effects on all trajectories, for each parameter p_i. These quantities are given by:

$$\mu_i = \frac{1}{\Psi} \sum_{j=1}^{\Psi} \mid d^{(i,j)} \mid \quad ; \quad \sigma_i = \sqrt{\frac{1}{\Psi} \sum_{j=1}^{\Psi} (d^{(i,j)} - \mu_i)^2} \tag{18}$$

Finally, a graphical analysis where μ_i is reported on the x-axis and σ_i on the y-axis enables to distinguish between parameters with low influence (close to the origin), parameters with linear influence on the output (close to the x-axis), parameters with non-linear influence or with strong interaction with others (close to the y-axis). This way, the set $\boldsymbol{p}$ is reduced to a subset $\boldsymbol{p'}$ containing only parameters with high influence, which considerably reduces the complexity of the identification procedure.

2.2.3. Parameter identification

The optimization problem addressed in our context is non-convex, non-linear, non-differentiable and does not have a unique solution. Indeed, the studied system is weakly observable, meaning that the internal states (cardiac signals) cannot be inferred directly from only one or only few target ECGs. The purpose here is to find a solution that is satisfying regarding the constraints that have been imposed in equation (15). An appropriate algorithm for solving this problem

is one that does not require the existence of the derivative of the cost function with respect to parameters, adapted to complex problems with potentially multiple local optima, and robust. For these reasons, heuristic-based approaches, particularly Evolutionary Algorithms (EAs) [34, 35] are more suitable than classical deterministic algorithms. EAs are guided random search approaches that originate from genetic algorithms [36].

Evolutionary Algorithms (EAs) are inspired by the evolution theory in which the strongest organisms are the ones that survive in the future generations. It was supposed that the solution of problem (16) could be encoded by a set of parameters, called genes. Each set $\boldsymbol{p}$ is represented by a vector of genes called chromosome. A generation can be defined by a population of several chromosomes. Following the principle of the survival of the fittest, the algorithm starts from an initial population $\boldsymbol{Pop}_0$ of N chromosomes $\boldsymbol{p}_0^j$, $j \in \{1..N\}$. Then, it evolves from one generation $\boldsymbol{Pop}_{i-1}$ to the next $\boldsymbol{Pop}_i$ through genetic operations referred to as mutations and crossovers. These operations are applied to a subset of $\boldsymbol{Pop}_{i-1}$, giving birth to new chromosomes $\boldsymbol{Pop}'_{i-1}$. Only the N fittest chromosomes in $\boldsymbol{Pop}'_{i-1}$ and $\boldsymbol{Pop}_{i-1}$ are kept to constitute the next population $\boldsymbol{Pop}_i$. In the original definition of genetic algorithms, genes are discrete values encoded in one bit. EAs are an extension to this concept in which genes are real valued. This entails defining an appropriate variation domain with an upper and a lower bound for each parameter. Convergence and robustness properties of EAs strongly depend on the cost function, the appropriate encoding of individuals, and the choice of genetic operators (see [37] for further reading). A pseudo-code of the used EA is given in Algorithm 2.

Algorithm 2 EA pseudo-code

Initialization: Provide a population $\boldsymbol{Pop}_0$ of N individuals and evaluate their associated cost
$i = 1$
while $i < N_{populations}$ **do**
  Select the best individuals from $\boldsymbol{Pop}_{i-1}$
  Create new individuals $\boldsymbol{Pop}'_{i-1}$ using crossover and mutation
  Evaluate each individual of $\boldsymbol{Pop}'_{i-1}$
  Create $\boldsymbol{Pop}_i$ by keeping the N best individuals of $\boldsymbol{Pop}'_{i-1} \cup \boldsymbol{Pop}_{i-1}$
  $i = i + 1$
end while

2.3. Inverse problem

Here, the epicardial source model is used for solving the inverse problem. Thus, the discretization of the forward problem using FEM yields the following linear system:

$$\boldsymbol{x} = \boldsymbol{G}\boldsymbol{s}^* + \boldsymbol{e} \tag{19}$$

where $\boldsymbol{x} \in \mathbb{R}^{M\times 1}$ is the vector of ECG potentials measured by the M sensors placed on the torso surface, $\boldsymbol{s}^* \in \mathbb{R}^{N\times 1}$ is the vector of heart surface potentials where N is the number of nodes on this surface, $\boldsymbol{G} \in \mathbb{R}^{M\times N}$ is the transfer matrix linking the sources $\boldsymbol{s}^*$ and the observations $\boldsymbol{x}$, and $\boldsymbol{e}$ an additional white Gaussian noise. The inverse problem of ECG consists in finding $\boldsymbol{s}^*$ given $\boldsymbol{x}$ and $\boldsymbol{G}$. This problem is ill-posed and Tikhonov regularization has been extensively used to minimize solution instability associated with this. It consists in finding the optimal $\hat{s}$ such that:

$$\hat{s} = \underset{\boldsymbol{s}^*}{\operatorname{argmin}} \quad \frac{1}{2}||\boldsymbol{G}\boldsymbol{s}^* - \boldsymbol{x}||_2^2 + \lambda||\boldsymbol{R}\boldsymbol{s}^*||_2^2 \tag{20}$$

$$= (\boldsymbol{G}^T\boldsymbol{G} + \lambda\boldsymbol{R}^T\boldsymbol{R})^{-1}\boldsymbol{G}^T\boldsymbol{x} \tag{21}$$

where $\boldsymbol{R} \in \mathbb{R}^{T\times N}$ is the regularization operator matrix. $\boldsymbol{R}$ can be the identity matrix $\boldsymbol{I}$ (zero order regularization) which limits the total magnitude of the solution, the spatial gradient operator $\boldsymbol{V}$ (first order regularization) that limits the solution steepness, or the spatial Laplacian operator $\boldsymbol{L}$ (second order regularization) that restricts steepness change. $\boldsymbol{V}$ maps the node space onto the edges space and plays the role of a spatial gradient by computing the amplitude difference between two nodes belonging to the same edge in the generated mesh. The Laplacian is defined as the difference between two neighboring edges. The notion of numerical neighborhood between two edges is considered in the sense that neighboring edges are all the couples of edges sharing one node. The first term of (20) is the data fidelity term, the second term is a regularization term that tends to constrain the magnitude of the solution or a linear transform of it, and λ is the so-called regularization parameter that represents the trade-off between data fitting and the

amount of regularization. The choice of the regularization parameter value is critical in regularization-based methods. Several classical methods attempt to provide a balance between the residual norm and the regularization weight. The most popular approaches are L-curve [19], U-curve [15], CRESO [16], GCV [17], RGCV [18] and DP [20].

For each of these methods, a panel of solutions is computed for a dense grid of λ. For each λ, $\hat{s}$ has to be computed and thus $\boldsymbol{G}^T\boldsymbol{G}+\lambda\boldsymbol{R}^T\boldsymbol{R}$ has to be inverted, which is time consuming and is subject to numerical errors. Thus, to analyze these different methods, the Generalized Singular Value Decomposition (GSVD) of the matrix pair $\{\boldsymbol{G},\boldsymbol{R}\}$ [17, 14] is used and an underdetermined case ($M \leq N \leq T$) is considered, such that:

$$\boldsymbol{G} = \boldsymbol{P}\begin{bmatrix}\boldsymbol{0} & \boldsymbol{\Sigma}_C\end{bmatrix}\boldsymbol{Z}^{-1}, \quad \boldsymbol{R} = \boldsymbol{Q}\begin{bmatrix}\boldsymbol{I} & \boldsymbol{0}\\ \boldsymbol{0} & \boldsymbol{\Sigma}_S\end{bmatrix}\boldsymbol{Z}^{-1}$$

where $\boldsymbol{P}$ and $\boldsymbol{Q}$ are orthonormal matrices, and $\boldsymbol{Z}$ is nonsingular. The regularized solution (21) can be written as:

$$\hat{\boldsymbol{s}} = \sum_{i=1}^{M}\frac{\tau_i^2}{\tau_i^2+\lambda}\frac{\boldsymbol{p}_i^T\boldsymbol{x}}{\sigma_i}\boldsymbol{z}_{i-(M-N)}$$

where σ_i and ϵ_i are the i^{th} diagonal elements of $\boldsymbol{\Sigma}_C$ and $\boldsymbol{\Sigma}_S$ respectively, τ_i is the i^{th} generalized singular values σ_i/ϵ_i, and $\boldsymbol{p}_i$ and $\boldsymbol{z}_i$ are the i^{th} columns of $\boldsymbol{P}$ and $\boldsymbol{Z}$ respectively. The two terms of the equation (21) can be rewritten as:

$$\boldsymbol{\eta}^2(\lambda) = \|\boldsymbol{R}\hat{\boldsymbol{s}}\|_2^2 = \sum_{i=1}^{M}\left(\frac{\tau_i}{\tau_i^2+\lambda}\right)^2(\boldsymbol{p}_i^T\boldsymbol{x})^2 \tag{22}$$

$$\boldsymbol{\rho}^2(\lambda) = \|\boldsymbol{G}\hat{\boldsymbol{s}}-\boldsymbol{x}\|_2^2 = \sum_{i=1}^{M}\left(\frac{\lambda}{\tau_i^2+\lambda}\right)^2(\boldsymbol{p}_i^T\boldsymbol{x})^2 \tag{23}$$

The advantage of the GSVD is that $\hat{s}$ does not need to be computed for each λ for the computation of $\boldsymbol{\rho}^2$ and $\boldsymbol{\eta}^2$. Consequently, the computations are simply much faster than when computing matrix inverses.

2.3.1. Optimal criterion

It is the most straightforward method for choosing the regularization parameter. This method consists in minimizing the Relative Error (RE) between the exact epicardial solution $\boldsymbol{s}^*$ and each of the regularized solutions $\hat{s}$ obtained by testing values of λ in a defined dense grid.

$$RE(\lambda) = \frac{\|\boldsymbol{s}^*-\hat{s}\|_2}{\|\boldsymbol{s}^*\|_2} \tag{24}$$

This method is clearly not feasible in practice since it requires the knowledge of the true solution but is convenient when the purpose is to evaluate inversion methods performance using simulated data.

2.3.2. L-curve

The L-curve plots the regularization norm $\|\boldsymbol{R}\hat{s}\|_2$ against the norm of the corresponding residual $\|\boldsymbol{G}\hat{s}-x\|_2$ in a log-log scale, both calculated for several regularization parameters λ. The optimal regularization parameter, $\hat{\lambda}$, is found in the corner of the curve:

$$L(\lambda) = (\log\boldsymbol{\rho}(\lambda), \log\boldsymbol{\eta}(\lambda)) \tag{25}$$

$\hat{\lambda}$ corresponds to the maximum curvature function defined as:

$$c(\lambda) = 2\frac{\hat{\boldsymbol{\rho}}'(\lambda)\hat{\boldsymbol{\eta}}''(\lambda)-\hat{\boldsymbol{\rho}}''(\lambda)\hat{\boldsymbol{\eta}}'(\lambda)}{(\hat{\boldsymbol{\rho}}'(\lambda)^2+\hat{\boldsymbol{\eta}}'(\lambda)^2)^{3/2}} \tag{26}$$

where $\hat{\boldsymbol{\rho}} = \log(\boldsymbol{\rho})$, $\hat{\boldsymbol{\eta}} = \log(\boldsymbol{\eta})$, $(')$ and $('')$ denote respectively the first and second order derivatives with respect to λ.

2.3.3. U-curve

This method plots the sum of the inverses of both the squared norm of the regularized solution, $\boldsymbol{\eta}^2$, and the squared norm of the residual, $\boldsymbol{\rho}^2$, as a function of λ in a log-log scale:

$$U(\lambda) = \frac{1}{\boldsymbol{\rho}^2(\lambda)}+\frac{1}{\boldsymbol{\eta}^2(\lambda)} \tag{27}$$

The U-curve is characterized by a decreasing part followed by an increasing part. $\hat{\lambda}$ is lying the corner between these two parts, and it corresponds to the maximum curvature point of the U-curve.

2.3.4. Composite REsidual and Smoothing Operator (CRESO)

The CRESO looks at the regularization parameter corresponding to the changes concavity at the first local maximum of the derivative of the difference between the penalty term and the squared norm of the residual $B(\lambda) = \lambda\boldsymbol{\eta}^2(\lambda) - \boldsymbol{\rho}^2(\lambda)$. It is calculated as follows:

$$\frac{\partial B(\lambda)}{\partial \lambda} = \boldsymbol{C}(\lambda) = \boldsymbol{\eta}^2(\lambda) + 2\lambda \frac{d}{d\lambda}\boldsymbol{\eta}^2(\lambda) \tag{28}$$

2.3.5. Generalized Cross Validation (GCV)

This method is based on the prediction of the observations arbitrarily excluded in the computation of regularized solution with the retained observations. So $\hat{\lambda}$ is chosen such that it minimizes the following generalized prediction error function:

$$GCV(\lambda) = \frac{\boldsymbol{\rho}^2(\lambda)}{\left(M - \sum_{i=1}^{M} \frac{\tau_i^2}{\tau_i^2+\lambda}\right)^2} \tag{29}$$

2.3.6. Robust Generalized Cross Validation (RGCV)

It has been shown that GCV can be unreliable for small or medium values of M, sometimes giving a low estimate. Therefore, proposed a new method making GCV more robust, involving a robustness parameter $\gamma \in [0, 1]$, and an approximate measure of the influence of each estimated point $\hat{s}$, $\mu(\lambda)$. The method consists of minimizing the following function:

$$RGCV(\lambda) = [\gamma + (1-\gamma)\mu(\lambda)]GCV(\lambda) \tag{30}$$

where $\mu(\lambda) = trace[(\boldsymbol{G}\boldsymbol{G}^{\#})^2] = \sum_{i=1}^{M} \frac{\tau_i^4}{(\tau_i^2+\lambda)^2}$.

2.3.7. Discrepancy principle

The discrepancy principle is a method that determines a value for $\mu(\lambda)$ when the noise variance is available. It states that satisfying solutions, $\hat{\lambda}$, are the ones lying in the set $\{\boldsymbol{\rho}^2(\hat{\lambda}) \leqslant c\}$, where c is computed from the noise variance.

3. Results and Discussion

This section first describes sensitivity analysis results and how they are exploited in order to reduce the set of model parameters. Then, quantitative and qualitative results in terms of convergence of the EA, 12-Lead ECGs shapes and characteristic features, action potential shapes and activation time mappings are provided and discussed. Three scenarios simulated by the obtained model are presented: one sinus-rhythm case, one ischemic case and one Ventricular Tachycardia (VT) case. Finally, the performance of Tikhonov-based regularization methods to solve the inverse problem on the presented scenarios are compared. A particular discussion will be focused on the choice of the regularization parameter.

3.1. Model reduction

To perform a sensitivity analysis of this model, a number of trajectories $\Psi = 370$ and a number of levels in each parameter variation grid $L = 50$ and a value of δ that represents two unitary displacements have been chosen in the uniform grid. In order to assess the robustness of this approach regarding the chosen ECG reference, the sensitivity analysis has been performed with respect to five different sinus-rhythm ECG references (lead II) obtained from physionet [38] that have been filtered and resampled.

The obtained sensitivity graphs are presented in Fig. 3 and are categorized by region for better visualization. Note that both endocardium and epicardium parameters are represented in the same graph entitled "ventricles" because they have the same values for both regions, except for parameter e_{epi}. Note that the sensitivity graph of each regions is obtained by projecting the graphs obtained for five different model outputs (five ECGs) on a same 2D map.

A first global remark is that the instances of a symbol with different colors are located closely to each other on the graph. This leads to think that model sensitivity with respect to the selected parameters and cost function does not

depend on the chosen reference ECG. Another global remark is that most of parameters are not close to the ordinate axis, which means that their optimal value with respect to the cost function cannot be determined independently from other parameters. Regarding parameter relative behavior, parameter χ has the major influence on the model. Indeed, this parameter has a major influence on the velocity of the electrical wave and thus on the overall shape of the synthetized ECG. The same reasoning explains why membrane capacitance c_m and conductivity $\boldsymbol{\sigma}$ are of high influence. One can also notice that the level of influence is different depending on the considered heart region. The reason may be in the difference of roles of the different regions regarding the cost function: atria activity is linked to P wave amplitude and duration, purkinje fibers and ventricles intervene in the QRS complex and the T-wave, and other regions operate mainly on the delay between the P wave and the QRS. Based on this sensitivity analysis, two major conclusions can be drawn: i) it is an encouraging indicator regarding the validity of the defined cost function (15) and ii) some parameter influence can be neglected regarding ECGs simulated by this model.

In order to reduce the complexity of the parameter identification problem (see next section), the parameter set $\boldsymbol{p}$ has restricted to a subset $\boldsymbol{p}'$ containing only parameters with high influence. To do so, an empirical threshold of 45% of the maximum mean and standard deviation in the sensitivity graph has been chosen, and retain only the parameters whose mean and standard deviation exceed this threshold. These parameters correspond to the outside of the light brown quadrant in Fig. 3.

3.2. Parameter identification

The simulated surface ECGs are obtained following three main steps, which are: define a variation domain for each parameter in $\boldsymbol{p}$, identify the best parameter vector $\boldsymbol{p}^*$, and obtain the corresponding cardiac mapping. In the first step, a variation domain for each parameter in $\boldsymbol{p}$ is defined. Indeed, in order to run an EA, a prerequisite is the definition of the variation domain for each gene. To do so, a local study for each parameter is conducted. A large range of values for each parameter was predefined for a given vector set $\boldsymbol{p}$. Only one parameter was varied in its predefined range and Algorithm 1 was run until a degenerate solution is found. This is done successively for each parameter. The upper and lower values for which degenerate solutions are obtained are taken to be the upper and lower bounds of the corresponding parameter variation domain.

Regarding the second step, Algorithm 2 is now run for 100 generations and 200 chromosomes in order to identify the best parameter vector $\boldsymbol{p}^*$ according to the cost function (16). The mutation probability is set to 0.25 and the selection rate to 8%. The initial generation was constituted of 38 manually chosen individuals, and the other 162 are randomly chosen in the space of $\boldsymbol{p}$. After initialization, parameters with low influence on the basis of Fig. 3 are fixed to values that are associated with the best cost and remain unchanged in the rest of the identification process. This way, only the subset $\boldsymbol{p}^{*'}$ is subject to genetic operations in the course of the EA. Algorithm 1 using the optimal parameter set $\boldsymbol{p}^*$ to obtain and visualize the corresponding cardiac mappings, and solving (14) to compute the 12-Lead ECGs. Fig. 4A shows the boxplot of cost values variability (y-axis) through generations (x-axis). The red bar indicates the median of cost values at each generation, and the bottom and top edges of the box indicate 1^{st} and 3^{d} percentiles respectively. The whiskers above and below the boxes show the locations of minimum and maximum cost values, and outliers are plotted in grey '+' sign. A rapid decrease in the median cost occurs in the first generations and reaches a minimum cost of 0.13 in generation 100. The first generation contains randomly selected chromosomes in the variation domain of $\boldsymbol{p}$. This population contains parameter sets that are inadequate and produce infinite costs. It is interesting to see that these cases are rejected starting from generation 2. One can also notice that cost values are very close and don't evolve between generations 32 and 44, but a jump occurs around generation 44. This leads to think that the algorithm went out of a local minimum and that it is capable of exploring better solutions.

The last step consists in running Algorithm 1 using the optimal parameter set $\boldsymbol{p}^*$ to obtain and visualize the corresponding cardiac mappings, and solving (14) to compute the 12-Lead ECGs. In order to assess the model reduction relevance, Fig. 4B shows the reference ECG (plain blue), the best solution provided by the EA when the sought parameter set is reduced ($\boldsymbol{p}^{*'}$ plain red) and when it is not ($\boldsymbol{p}^*$ dashed yellow). Indeed, the results was completed by running the EA without reducing the set $\boldsymbol{p}^*$. Clearly, the synthetized ECGs have the same characteristic shape, which supports the idea that the proposed model reduction is relevant. One can see that duration constraints have been respected, as well as the general characteristic shape of the P wave, QRS complex and the T wave of the ECG signal. This is confirmed quantitatively by a correlation value that reaches 88%. Note that adding an additional layer to the ventricles in the heart geometry enables to produce a T wave with an appropriate duration because of the difference of repolarization times between the ventricular layers. Without the additional ventricular layer, the repolarization wave

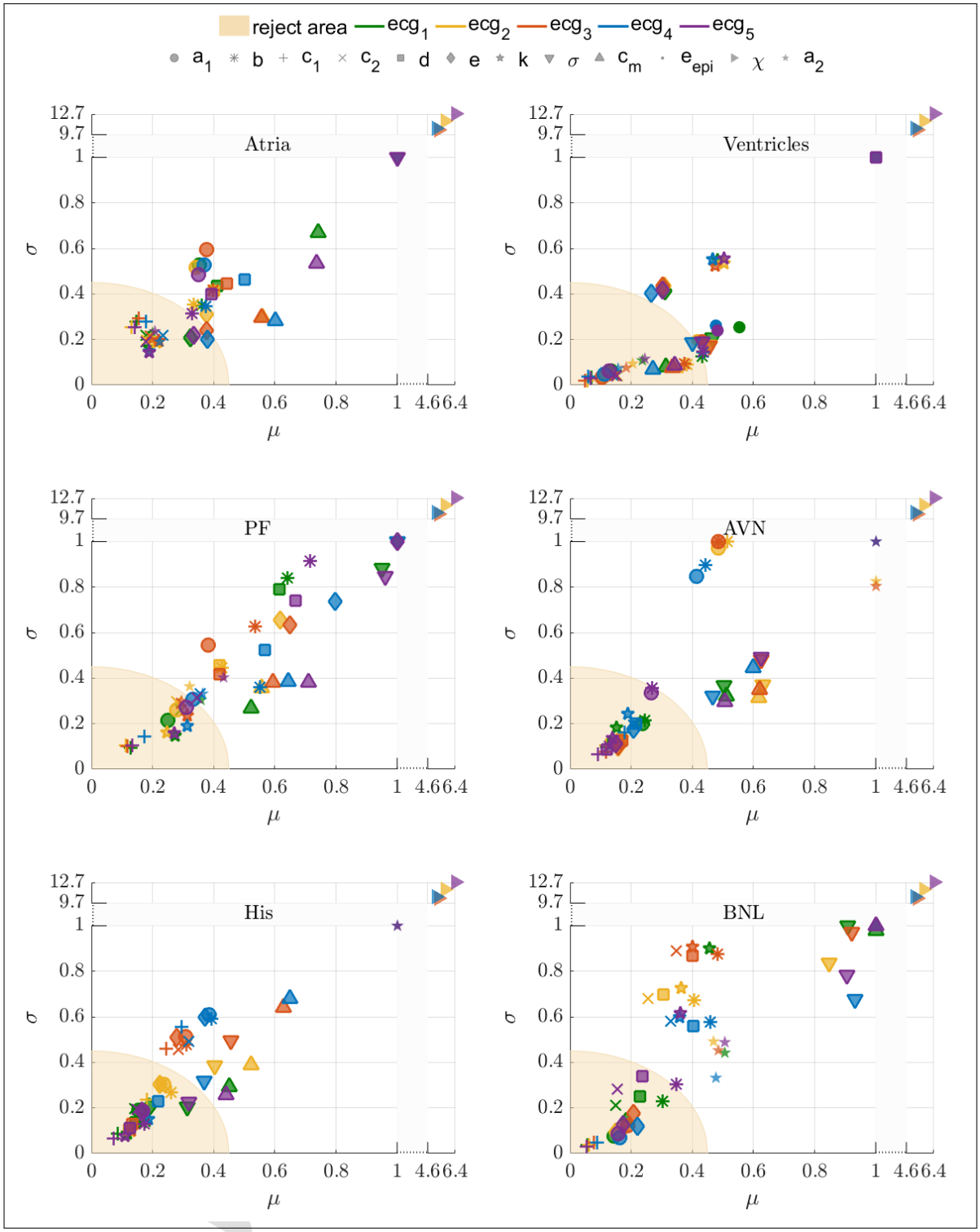

Figure 3: Sensitivity graph obtained for five different model outputs (each color corresponds to a different ECG reference) for all regions

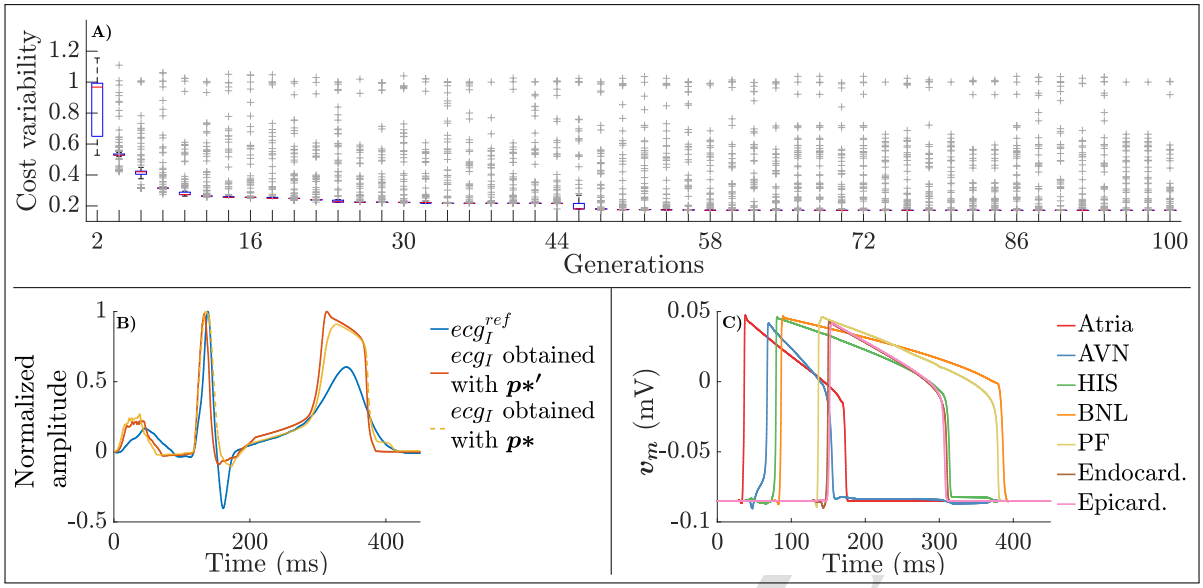

Figure 4: (A) Cost values evolution through generations. (B) Normalized ECG estimated by the EA (dashed yellow), best solution (plain orange) and reference ECG (plain blue). (C) Action potentials in the different cardiac regions.

in the ventricles would naturally be of the same speed as that of depolarization, which would give a much sharper, unrealistic T wave.

3.3. Physiological relevance

In this section, the simulation results in a normal scenario and two pathological scenarios (ischemia and ectopic VT) are analyzed. Ischemia is a disorder of cardiac function caused by insufficient blood flow to the heart's muscular tissues. It can lead to myocardial infarction, i.e. the death of myocardial muscle tissue. Tissue death implies that cells are no longer able to generate action potentials [1]. Here, ischemia was simulated by forcing action potentials in a delimited region of the right ventricle to remain at resting levels. Regarding the VT disorder, it is typically characterized by irregular contraction of the heart originating in the ventricles, preventing the heart from filling properly. It occurs when an electrical focus additionally to those in the SAN emits impulses. Two mechanisms can be the origin of VT: i) abnormal automaticity where cells in the ventricle become self-excitable and act as pacemaker cells; ii) scar related where most of scar area in the heart is dead and is thus electrically no conducting but some narrow electrical pathways form one or multiple mini re-entrant circuits spontaneously within the ventricular myocardium. In our case, the ectopic VT was simulated by forcing a stimulation at the apex, which causes a premature contraction of the ventricles.

Fig. 10 displays the Local Activation Time (LAT) mappings corresponding to the associated action potentials, and the 12-Lead ECGs. LATs are calculated from action potentials upstrokes. LAT mappings provide valuable functional and structural information about the initiation and the propagation pattern of cardiac electrical activity. It can be seen in the case of sinus rhythm (blue) that the general shape of action potentials and their durations globally match physiological knowledge. Only bundle branches action potentials are quite long compared to their average normal duration. In fact, since it is a relatively small region in the heart domain, action potentials duration in this region do not contribute much in the ECG shape. Information about their repolarization phase is difficult to integrate in the cost function and any variations in the repolarization phase of this region will not influence the simulated ECG shape. However, the depolarization wave speed is important and is well identified since it regulates the PR interval, which is a feature that is integrated in the cost function. Although the identification process was performed only in lead I, the general shapes of the rest of the 12-Lead ECGs agree well with morphological sinus-rhythm ECGs in terms of polarity and durations: the P wave polarity is positive in all ECGs except in aVR, and its duration is normally less or equal to 110ms. The QRS complex is represented by a positive deflection with a large, upright R in leads I, II, V4 - V6 and a negative deflection in aVR. Its duration is less or equal to 120 ms. The ST segment is isoelectric, sloping upwards to the T wave. The T wave polarity is the same as that of the QRS except in V2. In the ischemic scenario (orange), it can

[1] characteristic wave formed by the exchange of ions between the inside and outside of the nerve cell

be seen that the action potentials are quasi similar to those of sinus rhythm, except for the electrically passive region that simulates the infarct. On the LAT mapping, the blue part in the atria is the SAN region, whereas the blue part in the ventricles represents the area without electrical activity. In the ECG, an elevation of the ST segment in leads II, III, aVL, aVF V1 and V2 is clearly visible. These findings match their clinical usage as a diagnostic criterion of myocardial infarction. Concerning the ectopic VT scenario, action potentials in the atrial region are electrically inactivated. On the LAT mapping, the blue part in the ventricles represents premature stimulation at the apex, whereas the blue part in the atria corresponds to their inactivation during the cycle. On ECGs, the P wave is non-existent with a successive of QRST waves. Furthermore, the QRS complex is of less amplitude than the first healthy beat and is larger.

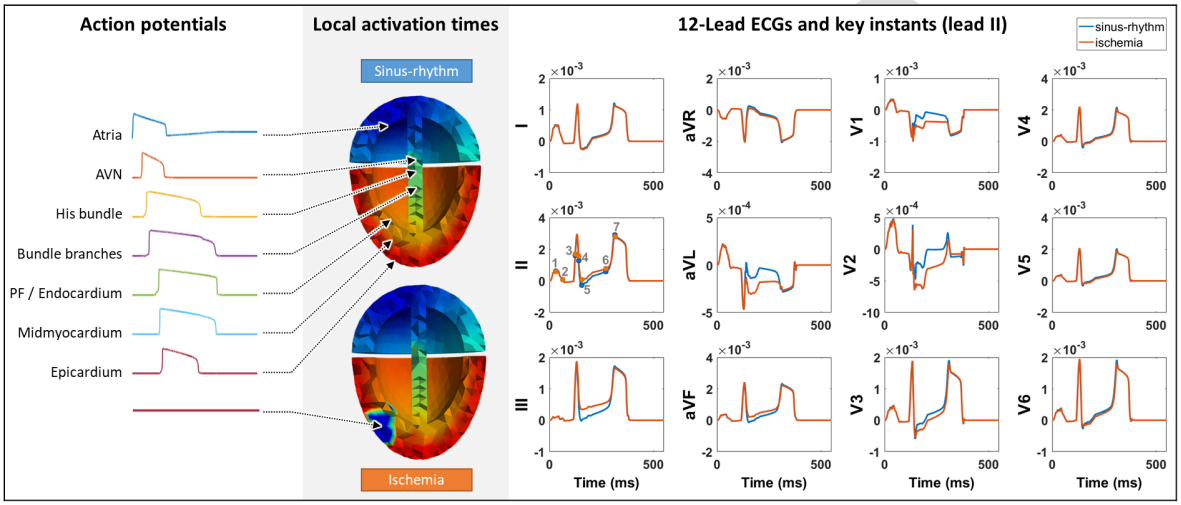

(A)

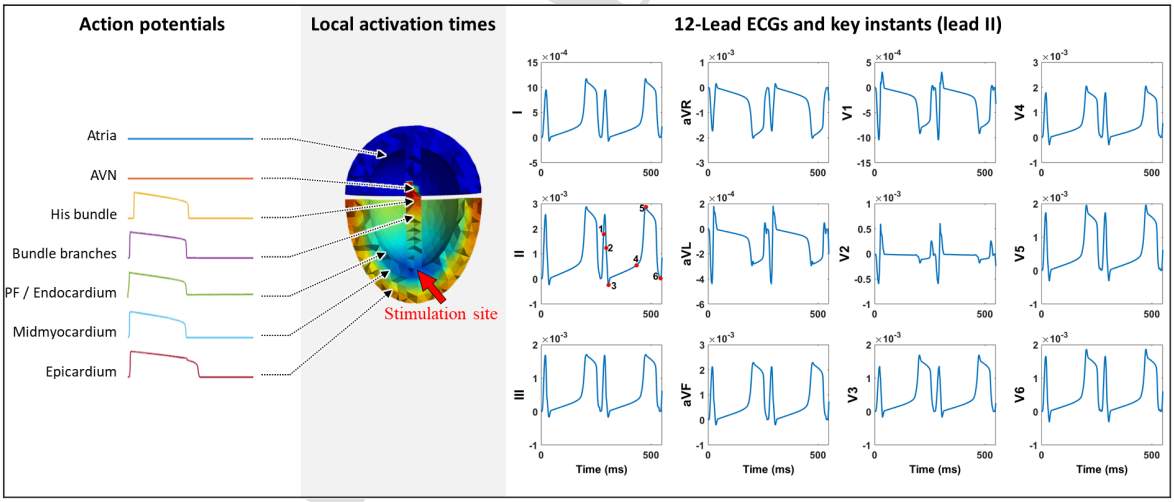

(B)

Figure 5: Local activation times with action potentials, simulated 12-Lead ECGs and key instants selected from Lead II for (A) sinus-rhythm and ischemia scenario, and (B) tachycardia scenario

3.4. Inverse problem simulations

In this section, numerical experiments conducted on data generated by the proposed model using different variants of Tikhonov-based inverse methods are described. More precisely, seven popular methods to choice the optimal regularization parameter were evaluated.

3.4.1. Performance evaluation

Several criteria are used for the evaluation of the performance of the tested methods. The first one is the Relative Error (RE), which is calculated from the estimated solution $\hat{s}(\lambda_{opt})$ and the exact one $\boldsymbol{s}^*$, in the same way as the optimal criterion (see (24)). The closer to zero the RE is, the better the performance is. The mean and the standard deviation of RE are calculated over 50 Monte Carlo (MC) simulations. Then, a success rate is calculated for each method by computing the number of times each algorithm returns a value between 0 and 1 for the RE. In addition, the behaviour of the methods through epicardial potential reconstructions mappings for a specific MC run has been illustrate. Then, the performance of the methods is quantitatively and qualitatively evaluated with the ground truth through all these criteria.

3.4.2. Data simulations

Simulations are performed on an ellipsoid heart and torso, where a tetrahedral mesh was generated. It must be noticed that, the level of refinement for the heart and torso meshes was fixed in order to have an adequate accuracy/complexity trade-off. Indeed, a mesh convergence analysis was performed by varying the number of nodes in the epicardial volume. In accordance with [8], from a certain threshold where the mesh was no longer considered coarse, the refinement of the mesh does not affect the generation of the 12-Lead ECGs, but increases the computation time. For instance, 6 shows the ECG of the Lead I for 4374 nodes (plain blue line) and 19830 nodes (dashed red line). It can be seen that, the generated ECGs are highly correlated. Thus, in our context, the heart domain mesh contains 4374 nodes (leading to 17418 elements) and 256-body surface measurements are randomly selected. As pointed before, three different scenarios has been simulated and a 10 dB additional white noise was considered for each of them. The variation grid for parameter λ takes 500 logarithmically equally spaced points between 10^{-24} and 10^{6}. The experiments are conducted on all instants of the ECG signals, but the results will focus on different key instants selected from lead II of the standard 12-Lead ECGs as shown in Fig. 10. Points 1 and 2 represent atrial depolarization (atrial contraction), points 3, 4, and 5 represent ventricular depolarization (ventricular contraction), while points 6 and 7 represent ventricular repolarization.

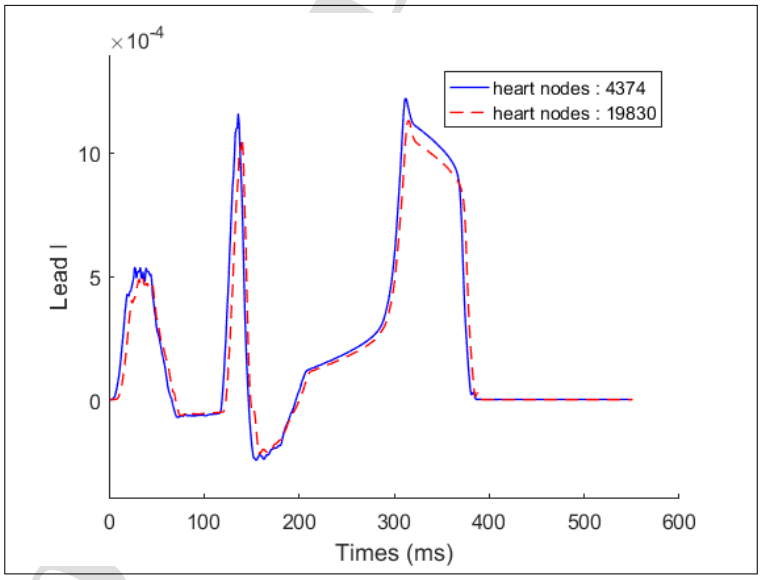

Figure 6: Comparison of two levels of refinement on the Lead I

3.4.3. Choice of the regularization operator

The first step in solving the inverse problem was to choose the regularization operator $\boldsymbol{R}$, i.e. $\boldsymbol{I}$, $\boldsymbol{V}$ or $\boldsymbol{L}$. Fig. 7 presents the RE values as a function of λ, at instants 1 and 3 of a sinus rhythm for the identity, the gradient and the laplacian operators. λ_{opt} was chosen based on the optimal criterion defined by (24). Results are in general slightly better when the gradient ($\boldsymbol{R} = \boldsymbol{V}$) is used. Thus for the rest of the study, $\boldsymbol{R} = \boldsymbol{V}$.

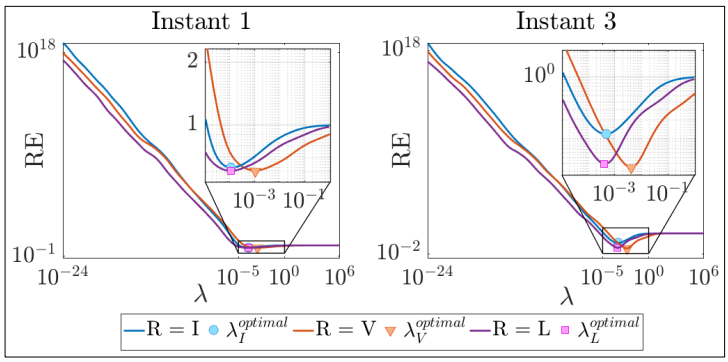

Figure 7: RE curves for the three-regularization operators $R = I$ (blue), $R = V$ (orange) and $R = L$ (purple) for instances 1 and 3, for the optimal criterion method

3.4.4. Regularization parameter calculation

The seven methods mentioned above was applied for the choice of the regularization parameter, namely: optimal criterion, L-curve, U-curve, CRESO, GCV, RGCV and DP. For example, Fig.8 depicted the curves of these methods as function of λ for time instant 3. It can be seen that the automatic choices of the regularization parameter ($\hat{\lambda}$) is recovered at the desired location, i.e. at the corner of the L-curve, at the first local maximum for CRESO, at the minimum of the functions for U-curve, GCV and RGCV, and finally at the intersection of the two curves for the DP. Note that, for the U-curve method, the optimal $\hat{\lambda}$ is different then those of the other methods.

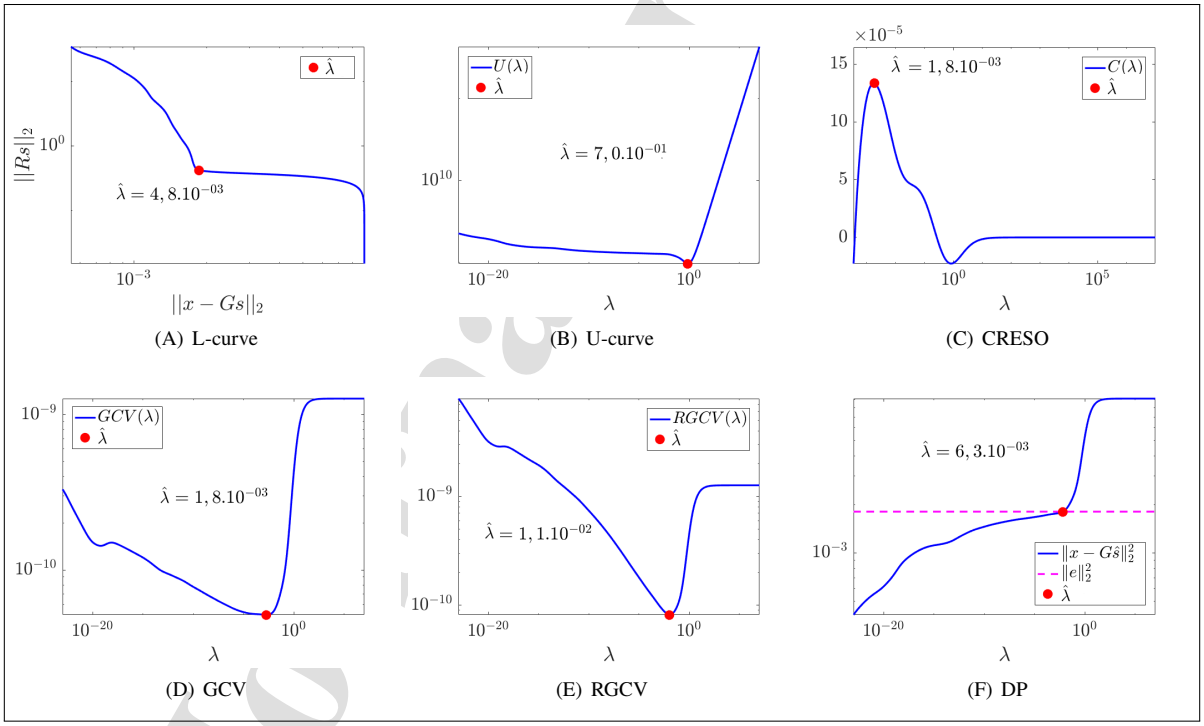

Figure 8: $\hat{\lambda}$ estimated using (A) L-curve, (B) U-curve, (C) CRESO, (D) GCV, (E) RGCV and (F) DP for time instant 3

Fig. 9A shows a box plot representing the success rate for the different methods computed over 50 MC runs. The first remark is that, for the L-curve, U-curve and CRESO methods, the results are poor (the median is lower than 60 %), i.e. they do not always succeed in determining an appropriate regularization parameter λ. Among the other methods, the RGCV and DP algorithms offer quasi-equivalent behaviors with respect to the optimal criterion and perform better than the other approaches with a quasi-perfect success rate. Regarding GCV, it gives intermediate

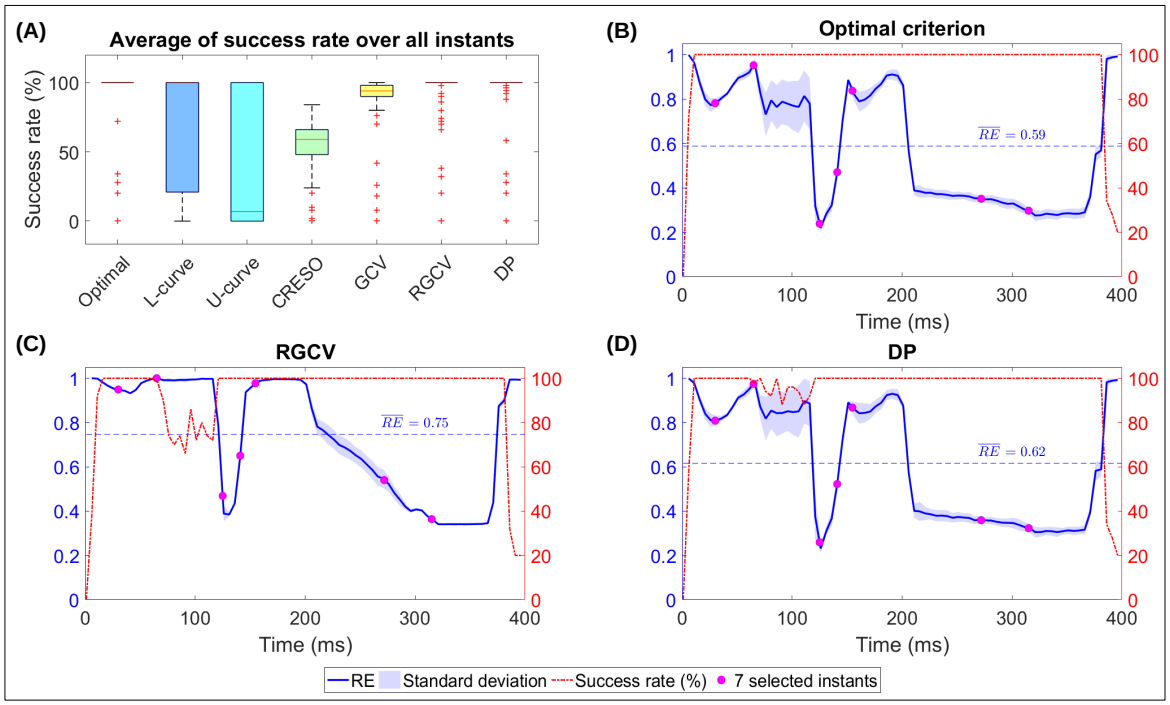

Figure 9: (A) Box plot of success rate for the 7 methods. (B)-(D) Graphical representation of mean of RE and success rate for optimal criterion, RGCV and DP methods in the case of sinus-rhythm

results with a median success rate greater than 85% and a small disparity. This first experiment clearly shows that the RGCV and DP algorithms, as the optimal method, provide less aberrant results than the other techniques in the studied context. Therefore, for all subsequent experiments, only the RGCV and DP methods will be considered.

Fig. 9B-D show the RE as a function of time (blue), as well as the success rate (red). Notice that the error curve, whatever the method, is inversely proportional to the ECG amplitude. This is due to the fact the power noise is the same for all instants. In other words, the SNR varies as a function of the ECG amplitude. Globally, RGCV and DP behave as the optimal method. More particularly, DP is a bit more efficient than RGCV: the RE of RGCV and DP, averaged over the 400 time instants, are equal to 0.75 and 0.62, respectively. In Fig. 11 (in Appendix), an example of epicardial mapping of the reference and the estimated solutions using optimal criterion, RGCV and DP are depicted for all time instants. The estimated mappings are globally in line with the quantitative results: optimal criterion, RGCV and DP give quasi-similar performance. Moreover, results obtained at time instant 3, 4, 6 and 7 are very close to the reference whereas the solutions obtained at instant 1, 2 and 4 do not correspond to the reference. As pointed before, this is essentially due to the fact that the local SNRs of instants 1 and 2 (atrial contraction), and 5 (at the level of S-wave), are lower than that of the rest instants.

3.4.5. Investigating pathological cases

This section can be viewed as a proof of concept, where the interest of the proposed method heart-torso to validate the ECGI methods for different pathological cases is highlighted. To do so, three previous pipelines (Tikhonov regularization combined with the optimal criterion, RGCV and DP) are applied on two pathological scenarios, namely ischemia and ectopic VT. As for the first experiment, the global SNR is set to 10 dB and the number of MC runs is fixed to 50. In both scenarios, the results presented in Fig. 10 are in line to those obtained on the sinus rhythm. Indeed, RE is inversely proportional to the local SNR. The global RE of RGCV and DP, averaged over all time instants, are equal to: i) 0.75 and 0.65 respectively for the ischemia, and ii) 0.71 and 0.47 respectively for VT. These results are also confirmed when visualizing an example of estimated epicardial mappings (Fig. 12 and Fig. 13 in Appendix). For instance, the visual inspection of the estimated mappings at time instant 5 (Fig. 12) shows clearly that the computed inverse solutions are not able to precisely delineate the ischemic region, whatever the used pipeline. This can be explained by the fact that the Tikhonov regularization leads to a blurred solution, which is not expected in the ischemic case. As far as the

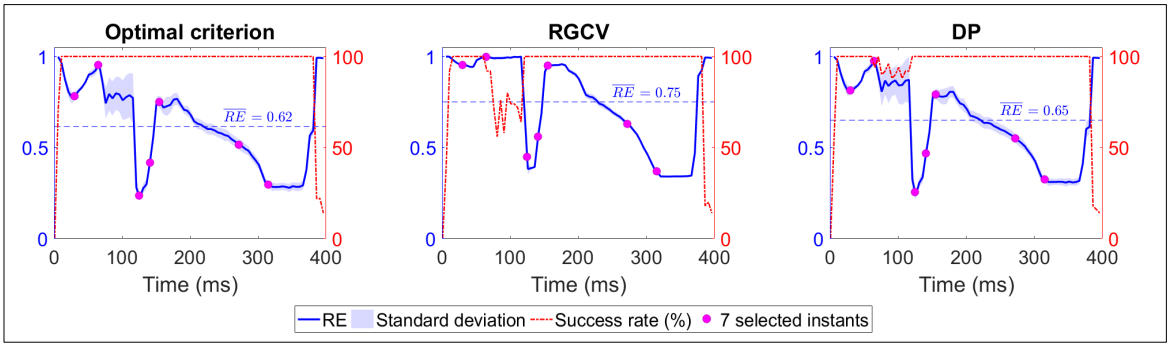

(A)

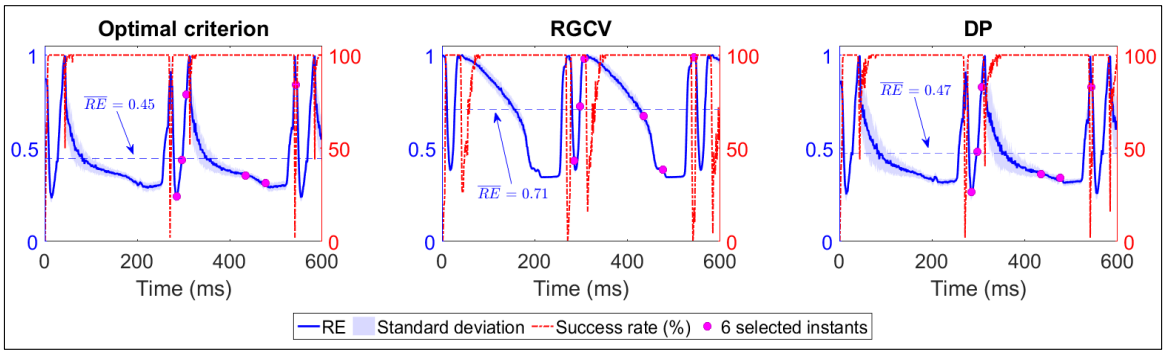

(B)

Figure 10: RE and success rate for the optimal criterion, RGCV and DP methods in the case of (A) ischemia and (B) ectopic VT

VT scenario is concerned, it can be seen that the estimated mappings of instants 3 and 6, which have very little energy, are note satisfactory whatever the used inverse method.

In the ectopic VT scenario, Fig. 10(B) shows that for instant 6, where the SNR is very low, performance is poor in both RE and success rate whatever the method is used. For the rest of the instances, the averaged RE results are relatively good, but with worse performance for instant 3 due to its SNR. The mappings (Fig. 13) show that the results returned by RGCV and DP are also quasi-similar for VT. For the instants 3 and 6, which have very little energy, the results are poor. Indeed, while no or very little energy is expected at the level of the atria, the reverse reconstruction shows electrical activity. Fig. 12 and Fig. 13 are appended in Annex for sake of place.

4. Limitations

Even if the obtained results are interesting, the proposed framework has some limitations. Clearly, there are some downside concerning the shape of the S and T waves. It could be observed that the amplitude of the T wave in the simulated ECG is much higher compared to the reference. This can be explained by a strong gradient between the ventricular layers. Indeed, since the action potential duration does not vary smoothly in the ventricular region as the repolarization front moves from the epicardium to the endocardium, an abrupt potential difference occurs in the boundary separating the layers, causing a T wave of higher amplitude. Note that adding an additional layer to the ventricles in the heart geometry therefore enables to produce a T wave with coherent duration. Without the additional ventricular layer, the repolarization wave in the ventricles would naturally be of the same speed as that of depolarization, which would give a sharp T wave as one can observe in [9]. In addition, the used of a geometry where both ventricles have the same size (which is not the case in practice) can also leads to a non-perfect shape of T-wave. As for the S wave, the influence of the electric axis of the heart is not studied in this work, which can explains its amplitude difference with the reference. Another limitation of this study is that sensitivity analysis is performed only for a sinus rhythm, it could be extended to other scenarios to explore model parameters that may be related to pathological cases. This

could improve the simulation of certain cardiac pathologies. Finally, the parameters identification, proposed for only one ECG lead and for a fixed resolution mesh, can be improved by exploiting more ECG leads and using several mesh finesses.

5. Conclusion and perspectives

This paper provides a simplified, fast, controllable and evolving 3D heart torso model, intended to perform quantitative evaluations of inverse methods on simulated data. The exploitation of the monodomain formalism and the FHN phenomenological model allow for a fast generation of ECG signals. Region-dependent model parameters, characterizing the electrical properties of the main anatomical structures of the heart are used in order to well represent the propagation of cardiac electrical activity. This study details the parameter identification process that has been used in order to generate ECG signals that best fit a given ECG reference. It is shown that, by proposing an adequate cost function it is feasible to reproduce the main temporal features and the general aspect of an observed real ECG. A sensitivity analysis of the monodomain model with respect to its parameters is also given to identify the FHN parameters having the highest influence on the generated cardiac electrical activity. This identification process succeeds in giving the same solution when only these highly sensitive parameters are identified, and also suggests that the results are reproducible for different healthy ECGs. Moreover, it is noteworthy to mention that the use of the FEM formalism allows us to consider anisotropic structures and the simplified geometry offers the possibility to easily study the influence of some modeling errors over the ECGI method performance, such as errors due to the considered mesh resolution. Finally, using this model, it is possible to consider several source formulations when dealing with the inverse problem. Indeed, it provides volumetric transmembrane potentials as well as epicardial potentials.

The second part of the paper presents a comprehensive study of Tikhonov regularization-based methods for solving the ECG inverse problem and shows the utility of such a low-resolution 3D model to evaluate the performance of ECGI methods. More particularly, the influence of the considered methods for choosing an adequate regularization parameter is studied and the results show that the Tikhonov method with RGCV or DP are more efficient in the studied context. Note that the RGCV method has already been identified as an efficient method to estimate the penalty parameter [14]. The application of the best inverse pipelines on realistic pathological activation patterns, such as ischemia and VT underline the interest of the proposed model to analyze the behavior of inverse methods in different situations. For example, it has been shown that the Tikhonov regularization-based methods do not succeed in the case of lower SNR values and/or pathological ECG signals. All obtained results demonstrate that the proposed low-resolution 3D heart torso model is an interesting and promising signal generator in the context of ECG inverse method evaluation.

According to the limitation section, some perspectives of this work can be distinguished between the cardiac modeling part and the inverse problem part. Regarding the modeling part, the sensitivity analysis could be extended in order to explore model parameters that can be linked to pathological cases. This can serve to better identify the model parameters for simulating certain cardiac pathologies. In addition, as mentioned previously, only one ECG lead (lead II) and one fixed mesh resolution are exploited to identify the optimal parameter set that generate the more realistic EGCs. Further improvements will consist in studying the influence of both the number of the reference ECG leads and the resolution mesh used to maximize similarity measure between a real ECGs and the ones simulated by our model. This could lead to the generation of a more accurate ST-segment. Regarding the ECG inverse problem, further work is warranted on investigating the behavior of other approaches for solving the ECG inverse problem.

Acknowledgment

This work was supported in part by the company ANSYS, Brittany Region (ARED funding) and the engineering school Ecole Centrale Nantes.

Appendix: Mapping figures

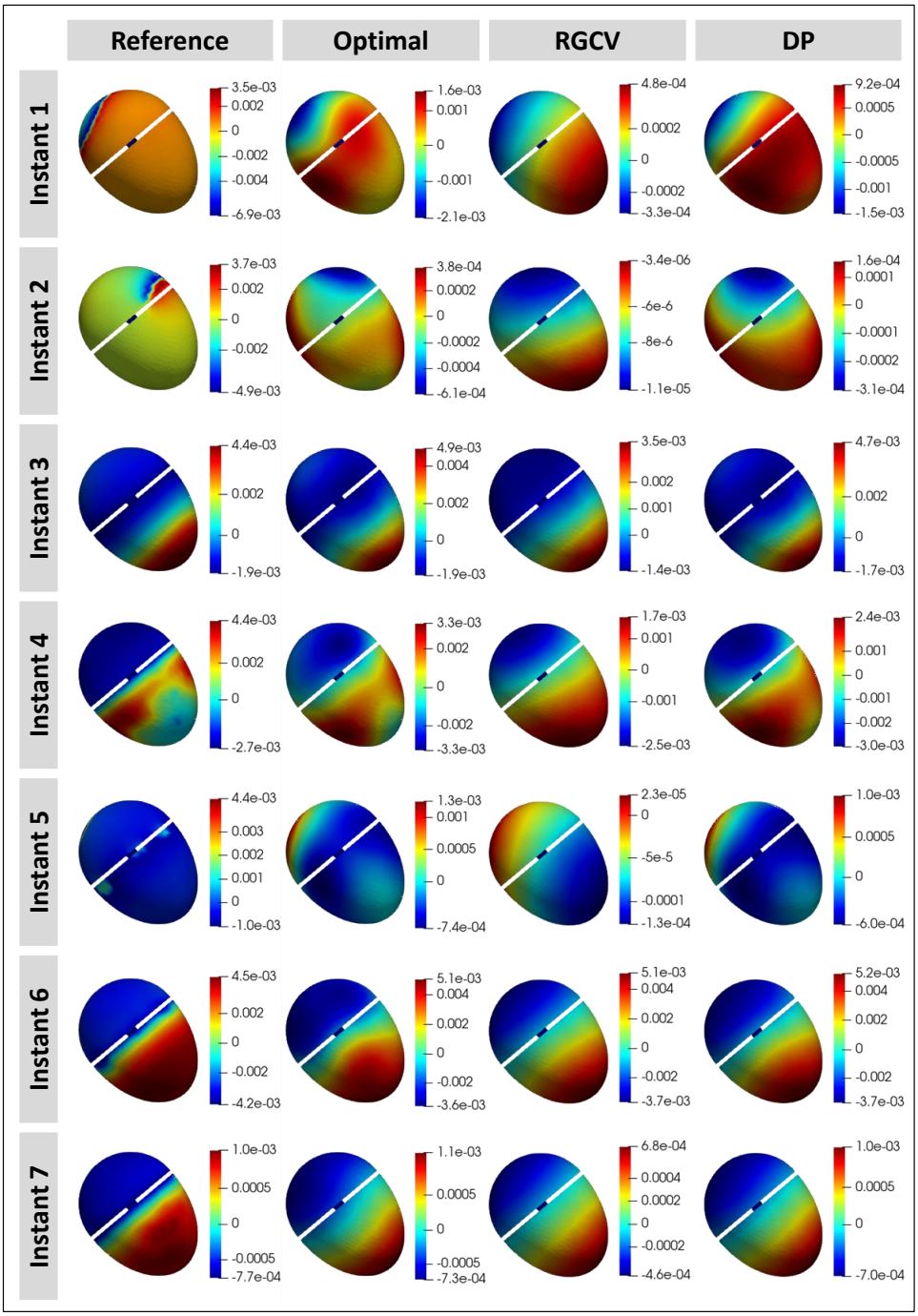

Figure 11: Estimated epicardial mapping with the optimal regularization parameter of optimal criterion, RGCV and DP methods in the case of sinus-rhythm

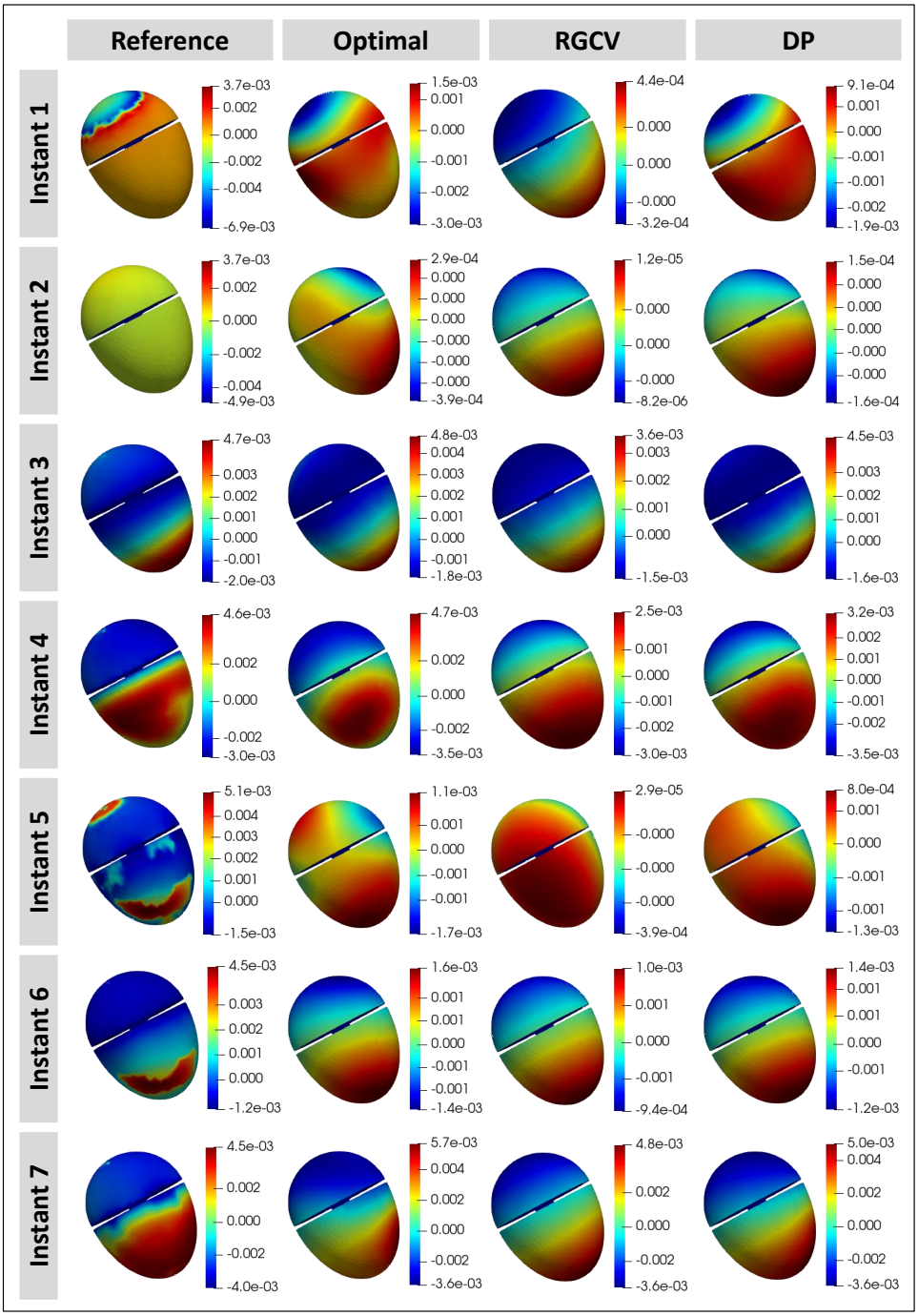

Figure 12: Estimated epicardial mapping with the optimal regularization parameter of optimal criterion, RGCV and DP methods in the case of ischemia

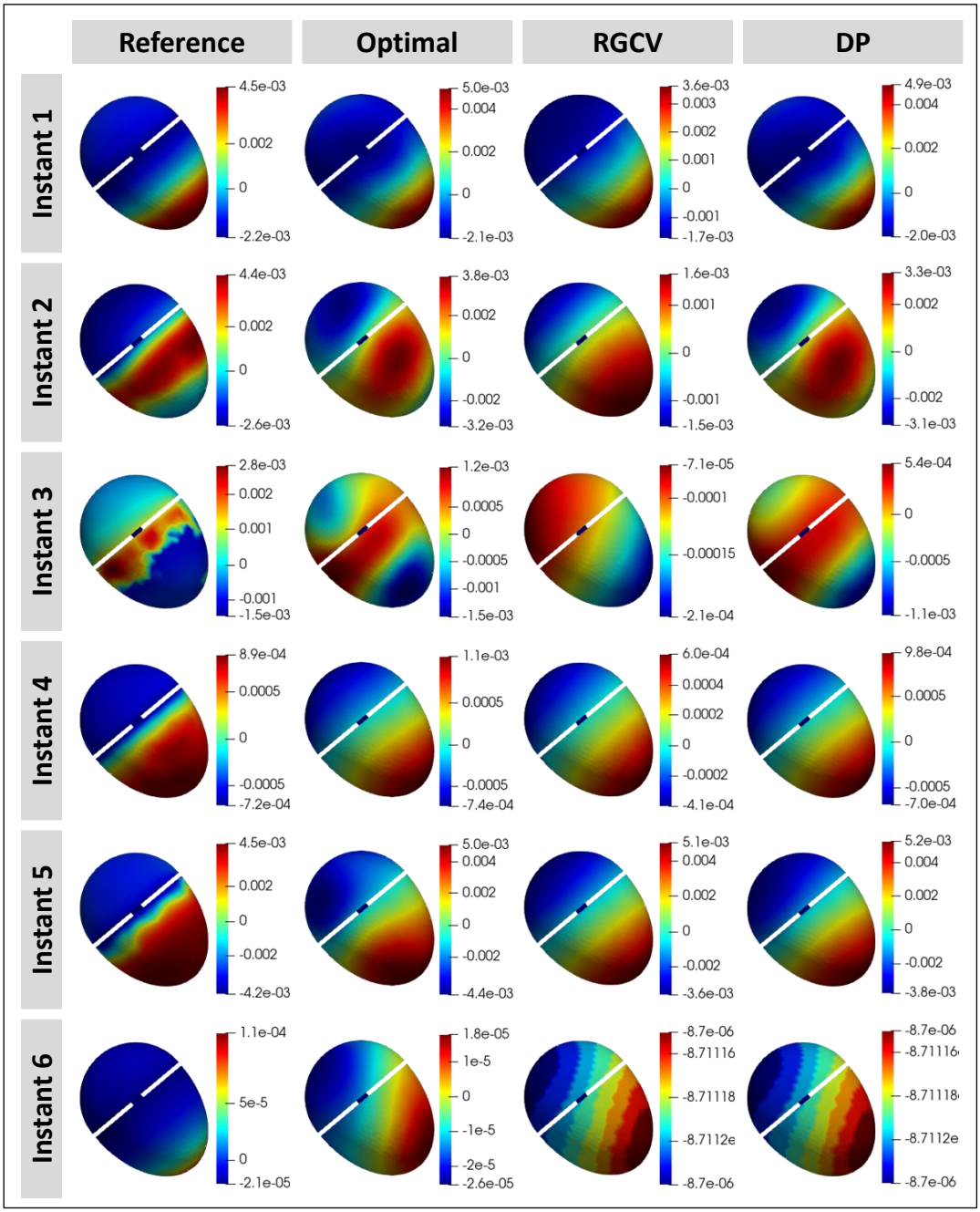

Figure 13: Estimated epicardial mapping with the optimal regularization parameter of optimal criterion, RGCV and DP methods in the case of TV

References

[1] E. J. Benjamin, P. Muntner, M. S. Bittencourt, Heart disease and stroke statistics-2019 update: a report from the american heart association, Circulation 139 (2019) e56–e528.

[2] G. J. Wynn, M. El-Kadri, I. Haq, M. Das, S. Modi, R. Snowdon, M. Hall, J. E. Waktare, D. M. Todd, D. Gupta, Long-term outcomes after ablation of persistent atrial fibrillation: an observational study over 6 years, Open Heart 3 (2016) e000394.

[3] L. Bear, M. Cluitmans, E. Abell, J. Rogier, L. Labrousse, L. Cheng, I. LeGrice, N. Lever, G. Sands, B. Smaill, M. Haïssaguerre, O. Bernus, R. Coronel, R. Dubois, Electrocardiographic imaging of repolarization abnormalities, Journal of American Heart Assoc. (2021).

[4] L. Bear, I. LeGrice, G. Sands, N. Lever, D. Loiselle, D. Paterson, L. Cheng, B. Smaill, How accurate is inverse electrocardiographic mapping? a systematic in vivo evaluation, Circ Arrhythm Electrophysiology (2018).

[5] G. T. Lines, M. L. Buist, P. Grottum, A. J. Pullan, J. Sundnes, A. Tveito, Mathematical models and numerical methods for the forward problem in cardiac electrophysiology, Computing and Visualization in Science 5 (2003) 215–239.

[6] B. Pfeifer, M. Seger, F. Hanser, C. Hintermüller, G. Fischer, H. Mühlthaler, B. Tilg, A training whole-heart model for simulating propagation and ecg patterns, Biomedical Signal Processing and Control 2 (2007) 323–330.

[7] J. C. Clements, J. Nenonen, P. K. J. Li, B. M. Horáček, Activation dynamics in anisotropic cardiac tissue via decoupling, Annals of biomedical engineering 32 (2004) 984–990.

[8] M. Boulakia, S. Cazeau, M. A. Fernández, J. F. Gerbeau, N. Zemzemi, Mathematical modeling of electrocardiograms: a numerical study, Annals of biomedical engineering 38 (2010) 1071–1097.

[9] S. Sovilj, R. Magjarevi, N. H. Lovell, S. Dokos, A simplified 3D model of whole heart electrical activity and 12-lead ECG generation, Computational and Mathematical Methods in Medicine 2013 (2013).

[10] N. Biasi, A. Tognetti, Modelling whole heart electrical activity for ischemia and cardiac pacing simulation, Health Technol. (2020) 851–852.

[11] K. Gillette, M. A. F. Gsell, M. Strocchi, T. Grandits, A. Neic, M. Manninger, D. Scherr, C. H. Roney, A. J. Prassl, C. M. Augustin, E. J. Vigmond, G. Plank, A personalized real-time virtual model of whole heart electrophysiology, Frontiers in Physiology 13 (2022).

[12] M. J. Bishop, G. Plank, Bidomain ecg simulations using an augmented monodomain model for the cardiac source, IEEE transactions on biomedical engineering 58 (2011) 2297–2307.

[13] M. D. Morris, Factorial sampling plans for preliminary computational experiments, Technometrics 33 (1991) 161–174.

[14] A. Karoui, L. Bear, P. Migerditichan, N. Zemzemi, Evaluation of fifteen algorithms for the resolution of the electrocardiography imaging inverse problem using ex-vivo and in-silico data, Frontiers in Physiology 9 (2018).

[15] D. Krawczyk-Stańdo, M. Rudnicki, Regularization parameter selection in discrete ill-posed problems — the use of the u-curve, International Journal of Applied Mathematics and Computer Science 17 (2007) 157–164.

[16] P. C. Franzone, L. Guerri, B. Taccardi, C. Viganotti, Finite element approximation of regularized solutions of the inverse potential problem of electrocardiography and applications to experimental data, CALCOLO 22 (1985) 91–186.

[17] P. C. Hansen, Rank-Deficient and Discrete Ill-Posed Problems: Numerical Aspects of Linear Inversion, SIAM, 1998.

[18] M. A. Lukas, Robust generalized cross-validation for choosing the regularization parameter, Inverse Problems 22 (2006) 1883–1902.

[19] P. C. Hansen, Analysis of discrete ill-posed problems by means of the l-curve, SIAM Review 34 (1992) 561–580.

[20] V. A. Morozov, Methods for Solving Incorrectly Posed Problems, Springer New York, 1984.

[21] A. Inc., Introduction to Ansys DesignModeler, Version 18.0. URL: http://www.ansys.com/training-center/course-catalog/structures/introduction-to-ansys-designmodeler.

[22] A. Inc., Ansys mechanical enterprise, Version18.0. URL: https://www.ansys.com/training-center/course-catalog/structures/introduction-to-ansys-designmodeler.

[23] J. C. Neu, W. Krassowska, Homogenization of syncytial tissues., Critical reviews in biomedical engineering 21 (1993) 137–199.

[24] D. Noble, A. Varghese, P. Kohl, P. Noble, Improved guinea-pig ventricular cell model incorporating a diadic space, ikr and iks, and length-and tension-dependent processes., The Canadian journal of cardiology 14 (1998) 123–134.

[25] R. FitzHugh, Mathematical models of threshold phenomena in the nerve membrane, The bulletin of mathematical biophysics 17 (1955) 257–278.

[26] Y. Giga, N. Kajiwara, K. Kress, Strong time-periodic solutions to the bidomain equations with arbitrary large forces, arXiv preprint arXiv:1805.06813 (2018).

[27] P. Colli Franzone, G. Savaré, Degenerate evolution systems modeling the cardiac electric field at micro-and macroscopic level, in: Evolution equations, semigroups and functional analysis, Springer, 2002, pp. 49–78.

[28] Y. Bourgault, Y. Coudiere, C. Pierre, Existence and uniqueness of the solution for the bidomain model used in cardiac electrophysiology, Nonlinear analysis: Real world applications 10 (2009) 458–482.

[29] C. Rocsoreanu, A. Georgescu, N. Giurgiteanu, The FitzHugh-Nagumo model: bifurcation and dynamics, volume 10, Springer Science & Business Media, 2012.

[30] S. Dokos, S. L. Cloherty, N. H. Lovell, Computational model of atrial electrical activation and propagation, in: Engineering in Medicine and Biology Society, 2007. EMBS 2007. 29th Annual International Conference of the IEEE, IEEE, 2007, pp. 908–911.

[31] J. M. Rogers, A. D. McCulloch, A collocation-galerkin finite element model of cardiac action potential propagation, IEEE Transactions on Biomedical Engineering 41 (1994) 743–757.

[32] G. Duckett, D. Barkley, Modeling the dynamics of cardiac action potentials, Physical review letters 85 (2000) 884.

[33] D. Wang, R. M. Kirby, C. R. Johnson, Resolution strategies for the finite-element-based solution of the ecg inverse problem, IEEE Transactions on Biomedical Engineering 57 (2010) 220–237.

[34] J. H. Holland, Adaptation in natural and artificial systems: an introductory analysis with applications to biology, control, and artificial intelligence, MIT press, 1992.

[35] H. J. Bremermann, The evolution of intelligence: The nervous system as a model of its environment, University of Washington, Department of Mathematics, 1958.

[36] K. Sastry, D. Goldberg, G. Kendall, Genetic Algorithms, Springer US, Boston, MA, 2005, pp. 97–125. URL: https://doi.org/10.1007/0-387-28356-0_4. doi:10.1007/0-387-28356-0_4.

[37] H. Jun, Y. Xinghuo, Conditions for the convergence of evolutionary algorithms, Journal of Systems Architecture 47 (2001) 601 – 612. Evolutionary computing.

[38] A. L. Goldberger, L. A. N. Amaral, L. Glass, J. M. Hausdorff, P. C. Ivanov, R. G. Mark, J. E. Mietus, G. B. Moody, C.-K. Peng, H. E. Stanley, Physiobank, physiotoolkit, and physionet, Circulation 101 (2000) e215–e220.

- Design of a simplified, fast, controllable and evolving 3D heart torso model
- Identification of the most influential hyperparameters using a genetic algorithm
- Ability of the model to simulate several cardiac electrical behaviors
- A useful tool to evaluate the ECG problem inverse techniques

A reduced complexity ECG imaging model for regularized inversion optimization

Objectives

To propose a simplified, fast and evolutive model capable of simulating various scenarios of cardiac mappings in order to evaluate and compare the performance of inversion methods.

Step 1: Forward problem

Design of a low-resolution heart-torso model

Model reduction using sensitivity analysis

Parameter identification using an evolutionary optimization approach

Step 2: Simulation of various cardiac conditions

Sinus rhythm

Ischemia

Ventricular tachycardia

Step 3: Inverse problem

Methods for choosing the penalty parameter in Tikhonov regularization

L-curve

GCV

U-curve

RGCV

CRESO

Discrepancy principle

Conclusion

The results demonstrate that the proposed low-resolution 3D heart torso model is an interesting and promising signal generator in the context of ECG inverse method evaluation.

Manche, El Houari et al.
Computers in Biology and Medicine

Outcomes

Step 1

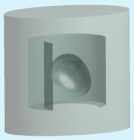

Heart-torso model

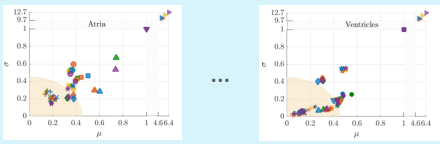

Sensitivity analysis: 58 → 25 parameters influent

Step 2

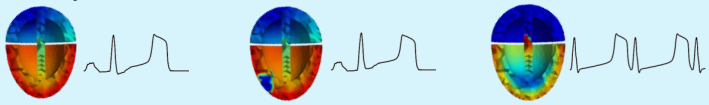

Sinus rhythm

Ischemia

Ventricular tachycardia

Step 3

Performance analysis of inverse methods for three scenarios: among the seven studied methods, RGCV and DP offer the best performances with quasi perfect **success rate**[1].

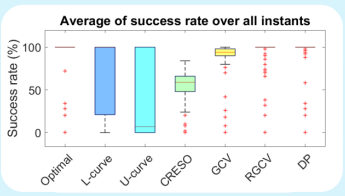

RE[2]	Sinus-rhythm	Ischemia	VT
RGCV	0,75	0,75	0,71
DP	0,62	0,65	0,47

[1] Number of times where the studied algorithm gives a reliable value of RE between 0 and 1
[2] Relative Error is calculated from the estimated solution and the exact one

Declaration of interests

☒ The authors declare that they have no known competing financial interests or personal relationships that could have appeared to influence the work reported in this paper.

☐ The authors declare the following financial interests/personal relationships which may be considered as potential competing interests: